Electronic Supplementary Information for

Heteroleptic Mononuclear Cu(I) Halide Complexes Containing Carbazolyl Substituted Phenyl Diphosphine and Monophosphine: Structures, Photophysical and Electroluminescent Properties

Zhun Chen[a,1], Wei Xu[a,1], Ruiqin Zhu[b,1], Li Liu[a,*], Xin-Xin Zhong[a,*], Fa-Bao Li[a,*], Guijiang Zhou[b,*], Hai-Mei Qin[c]

[a] *College of Chemistry and Chemical Engineering, Ministry of Education Key Laboratory for the Synthesis and Application of Organic Functional Molecules, Hubei University, Wuhan 430062, P. R. China. E-mail: liulihubei@hubu.edu.cn, xxzhong@hubu.edu.cn, lfb0615@hubu.edu.cn*

[b] *School of Chemistry, Xi'an Jiaotong University, Xi'an 710049, P. R. China. Email: zhougj@mail.xjtu.edu.cn*

[c] *Department of Chemistry, Xiamen University, Xiamen 361005, P. R. China.*

[1] These authors are contributed equally to this work.

CCDC: 2284138-2284139, 2282048-2282050, 2285410, 2323092

Contents

3. Molecular structures

4. Photophysical properties

λ_{em} = 556 nm for **6**, λ_{em} = 557 nm for **7**).

Figure 33. Time profiles of luminescence decay and exponential fit spectrum of **1** at 297 K (λ_{em} = 531 nm).

Figure S34. Time profiles of luminescence decay and exponential fit spectrum of **2** at 297 K (λ_{em} = 555 nm).

Figure S35. Time profiles of luminescence decay and exponential fit spectrum of **3** at 297 K (λ_{em} = 560 nm).

Figure S36. Time profiles of luminescence decay and exponential fit spectrum of **4** at 297 K (λ_{em} = 535 nm).

Figure S37. Time profiles of luminescence decay and exponential fit spectrum of **5** at 297 K (λ_{em} = 558 nm).

Figure S38. Time profiles of luminescence decay and exponential fit spectrum of **6** at 297 K (λ_{em} = 556 nm).

Figure S39. Time profiles of luminescence decay and exponential fit spectrum of **7** at 297 K (λ_{em} = 557 nm).

Figure S40. Time profiles of luminescence decay and exponential fit spectrum of **1** at 77 K (λ_{em} = 548 nm).

Figure S41. Time profiles of luminescence decay and exponential fit spectrum of **2** at 77 K (λ_{em} = 557 nm).

Figure S42. Time profiles of luminescence decay and exponential fit spectrum of **3** at 77 K (λ_{em} = 547 nm).

Figure S43. Time profiles of luminescence decay and exponential fit spectrum of **4** at 77 K (λ_{em} = 524 nm).

Figure S44. Time profiles of luminescence decay and exponential fit spectrum of **5** at 77 K (λ_{em} = 547 nm).

Figure S45. Time profiles of luminescence decay and exponential fit spectrum of **6** at 77 K (λ_{em} = 545 nm).

Figure S46. Time profiles of luminescence decay and exponential fit spectrum of **7** at 77 K (λ_{em} = 546 nm).

5. Computational details

Figure S47. Compositions of the frontier molecular orbitals at optimized S_0 geometry

of complex **1**.

Figure S48. Compositions of the frontier molecular orbitals at optimized S_0 geometry of complex **2**.

Figure S49. Compositions of the frontier molecular orbitals at optimized S_0 geometry of complex **3**.

Figure S50. Compositions of the frontier molecular orbitals at optimized S_0 geometry of complex **4**.

Figure S51. Compositions of the frontier molecular orbitals at optimized S_0 geometry of complex **5**.

Figure S52. Compositions of the frontier molecular orbitals at optimized S_0 geometry of complex **6**.

Figure S53. Compositions of the frontier molecular orbitals at optimized S_0 geometry of complex **7**.

Figure S54. Compositions of the frontier natural transition orbitals at optimized S_1 geometry of complex **1**.

Figure S55. Compositions of the frontier natural transition orbitals at optimized S_1 geometry of complex **2**.

Figure S56. Compositions of the frontier natural transition orbitals at optimized S_1 geometry of complex **3**.

Figure S57. Compositions of the frontier natural transition orbitals at optimized S_1 geometry of complex **4**.

Figure S58. Compositions of the frontier natural transition orbitals at optimized S_1 geometry of complex **5**.

Figure S59. Compositions of the frontier natural transition orbitals at optimized S_1 geometry of complex **6**.

Figure S60. Compositions of the frontier natural transition orbitals at optimized S_1 geometry of complex **7**.

Figure S61. Compositions of the frontier natural transition orbitals at optimized T_1 geometry of complex **1**.

Figure S62. Compositions of the frontier natural transition orbitals at optimized T_1 geometry of complex **2**.

Figure S63. Compositions of the frontier natural transition orbitals at optimized T_1 geometry of complex **3**.

Figure S64. Compositions of the frontier natural transition orbitals at optimized T_1

6. References

1. General information

All chemicals were purchased from commercial sources and used without being processed unless specified. Triphenylphosphine (PPh_3) was purchased from Energy Chemical Co. 1,2-bis(9-carbazolyl)-4,5-bis(diphenylphosphino)benzene (**DCzDP**) and 3-(diphenylphosphino)-9-methylcarbazole (**CzP**) were synthesized according to the literature methods.[1,2] Tetrahydrofuran (THF) was distilled under nitrogen in the presence of sodium chips with benzophenone as the indicator before use.

Instrumentation. ^{1}H, ^{13}C and ^{31}P NMR spectra were recorded on a Varian 400 MHz NMR spectrometer using deuterated solvents as the lock. Chemical shifts were reported in ppm relative to $SiMe_4$ for the ^{1}H, $CDCl_3$ for the ^{13}C, and 85% H_3PO_4 for the ^{31}P nucleus. High resolution mass spectra (HRMS) were recorded on the Thermo Scientific Exactive Plus equipped with ESI ionization source. The elemental composition was determined with SEM/EDS (Hitachi SU-800 FE-SEM). UV–vis absorption was recorded by a Unicam Helios α spectrometer. Emission spectra and lifetimes of the complexes were measured using Edinburgh instrument FLS980 steady-state and time resolved fluorescence spectrometer (375 nm variable pulsed diode laser, repetition frequencies 1000 Hz, and optical pulse period 100 ns). Solid-state Φ_{PL} values were determined using a Hamamatsu system for absolute PL quantum yield measurements equipped with an integrating sphere with Spectralon inner surface coating.

X-ray crystallography. Crystals of complexes **1**–**7** suitable for X-ray diffraction studies were grown by slow evaporation of CH_2Cl_2/*n*-hexane for **1–3**, CH_2Cl_2/CH_3CN for **4–6**, CH_2Cl_2/C_2H_5OH for **7** at room temperature. Geometric and intensity data were collected using Cu Kα radiation (λ = 1.54184 Å) on a XtaLAB Synergy,

Dualflex, HyPix area detector. The collected frames were processed with the software *SAINT*[3], and an absorption correction was applied (*SADABS*)[4] to the collected reflections. The structures were solved by direct methods (*SHELXTL*)[5] in conjunction with standard difference Fourier techniques and subsequently refined by full-matrix least-squares analyses on F^2. All non-hydrogen atoms were assigned with anisotropic displacement parameters.

Theoretical calculations. The structural parameters for complexes **1–7** were obtained from the crystal data which are listed in Tables 1 and S1. The corresponding ground-state (S_0) geometries were all optimized at theoretical level of B3LYP-D3(BJ)/6-311+G(d,p) (LANL2D2 for Cu and I atoms), where D3(BJ) was Grimme's D3 dispersion correction with Becke-Jonson damping. To calculate the adiabatic excitation energies, the optimized geometries of S_1 and T_1 are required, which were obtained at theoretical levels of TD-B3LYP-D3(BJ)/6-31+G(d) and UB3LYP-D3(BJ)/6-311+G(d,p) (LANL2D2 for Cu and I atoms), respectively. The absorption spectra based on the optimized S_0 geometries were obtained at the TD-B3LYP-D3(BJ)/6-311+G(d,p) (LANL2D2 for Cu and I atoms) level. In addition, the solvent effects were taken into account by the polarizable continuum model (PCM, solvent = dichloromethane) for the purpose of comparing with the experimental spectra. All the calculations were manipulated by the Gaussian 16 suite.[6] The compositions of the frontier molecular and natural transition orbitals at optimized S_0, S_1 and T_1 geometries of complex **1–7** were calculated by the Multiwfn program.[7,8]

Device fabrication. The pre-cleaned ITO glass substrates were treated with ozone for 20 min. Then, hole-injection layer of the PEDOT:PSS was spin-coated and cured at 120 °C for 30 min in the air. The emission layer was obtained by spin-coating a chloroform solution of complex **4** (x wt%) in 26DCzppy and TCTA (6:4) at different doping levels. After drying in a vacuum oven at 60 °C for 10 min, DPEPO, TmPyPB, LiF, and Al cathode were successively evaporated on the emission layer at a base pressure less than 10–6 Torr. The EL spectra were recorded with a PR650 spectra colorimeter. The J–V–L curves of the devices were measured by a Keithley 2400/2000 source meter. All the experiments and measurements were carried out under ambient conditions.

2. NMR and mass spectra

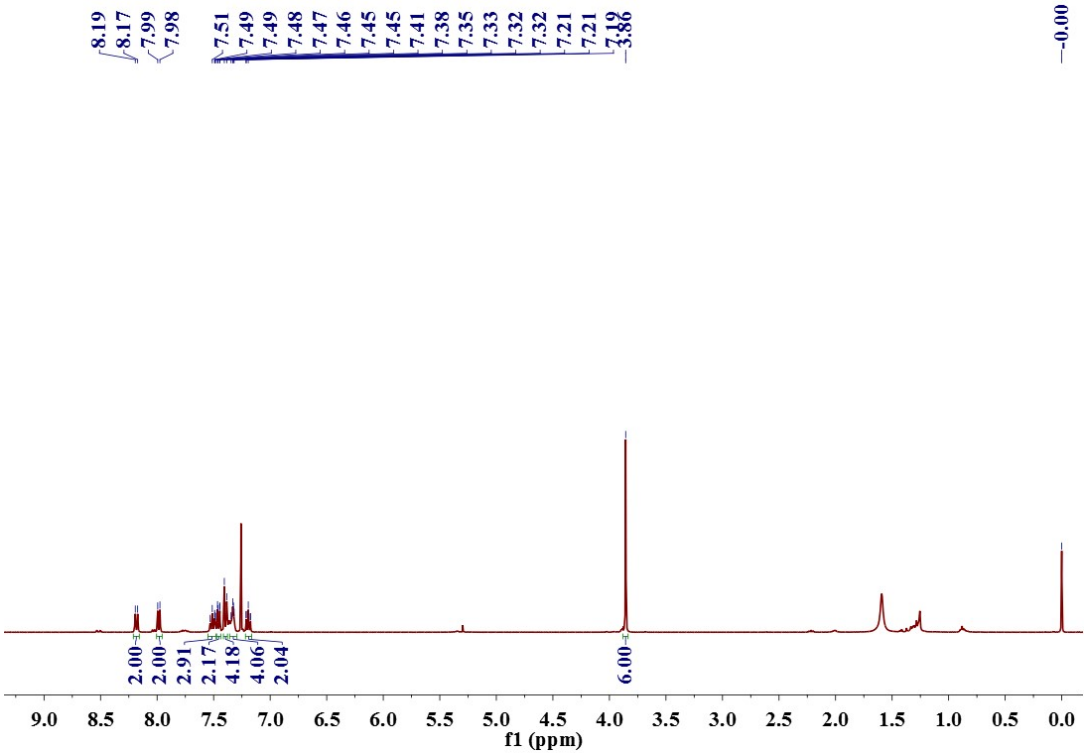

Figure S1. ^{1}H NMR spectrum of **DCzP** in $CDCl_3$.

δ = 5.30 (dichloromethane), 1.56 (H_2O), 0.88 and 1.26 (petroleum ether or hexane)

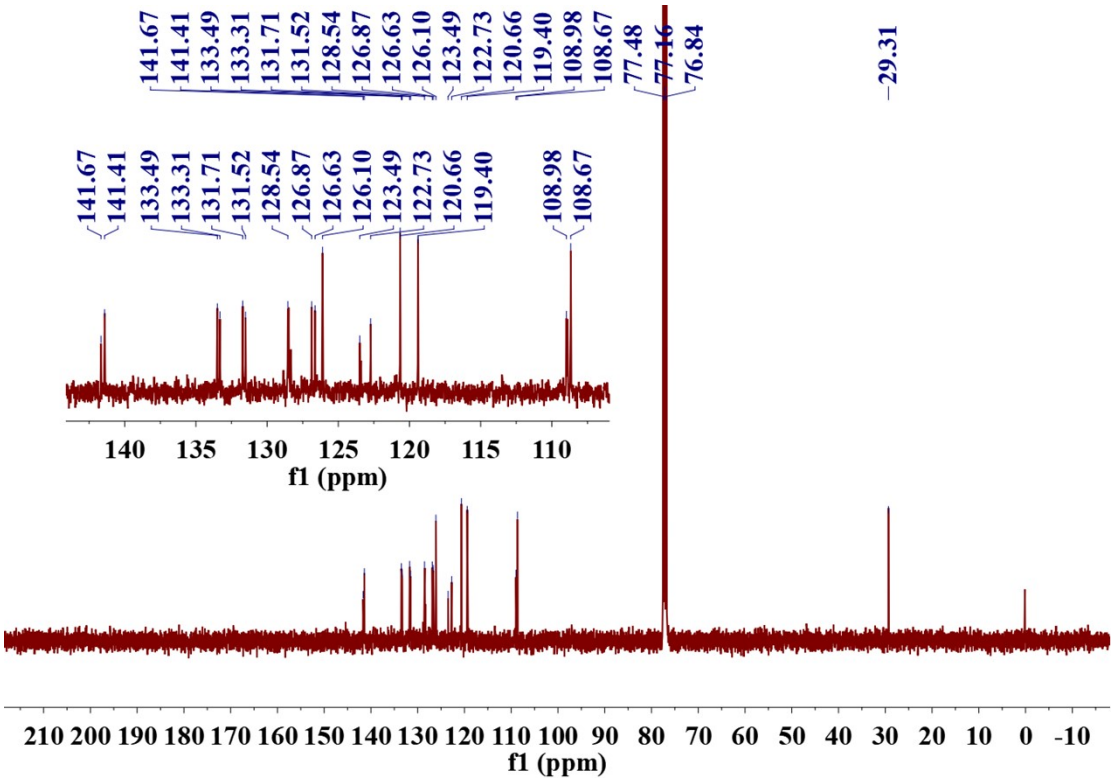

Figure S2. ^{13}C NMR spectrum of **DCzP** in $CDCl_3$.

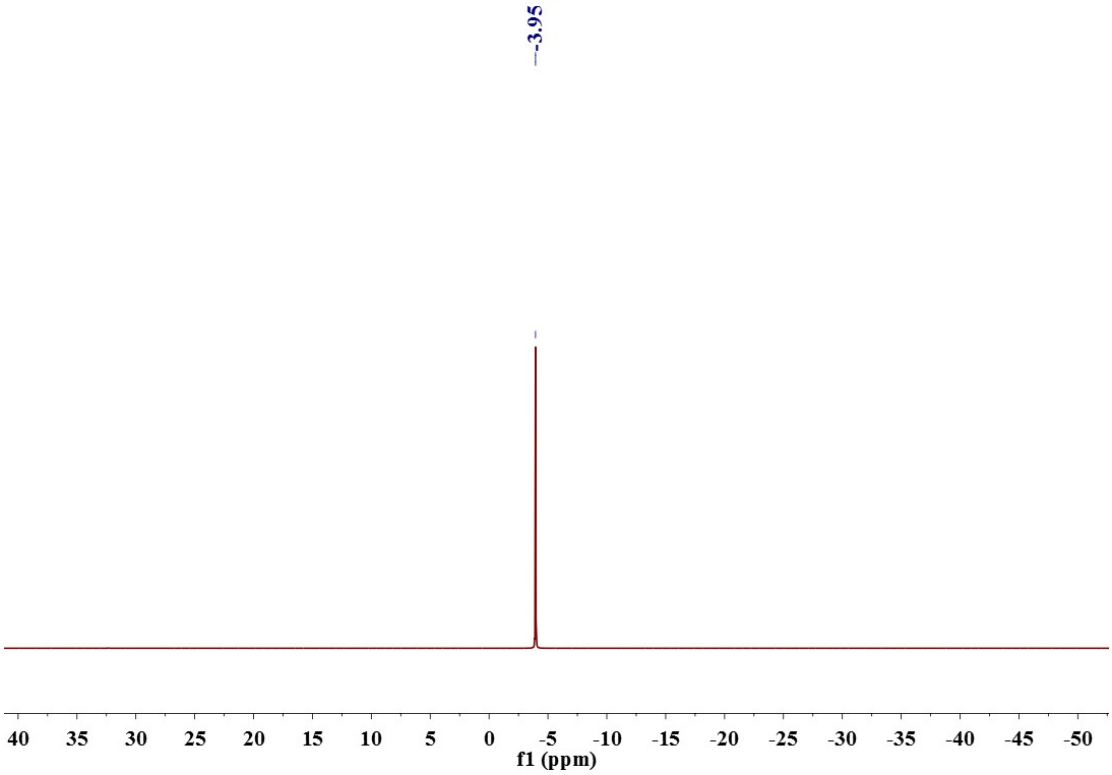

Figure S3. ^{31}P NMR spectrum of **DCzP** in $CDCl_3$.

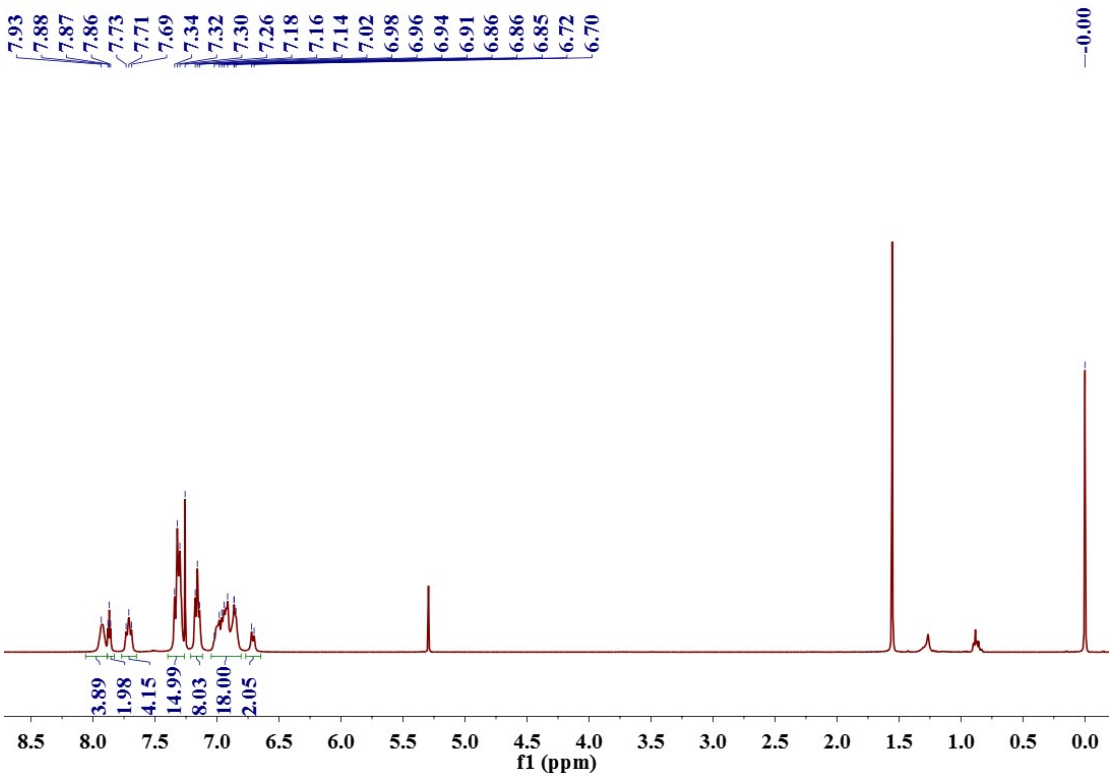

Figure S4. ^{1}H NMR spectrum of **1** in $CDCl_3$.

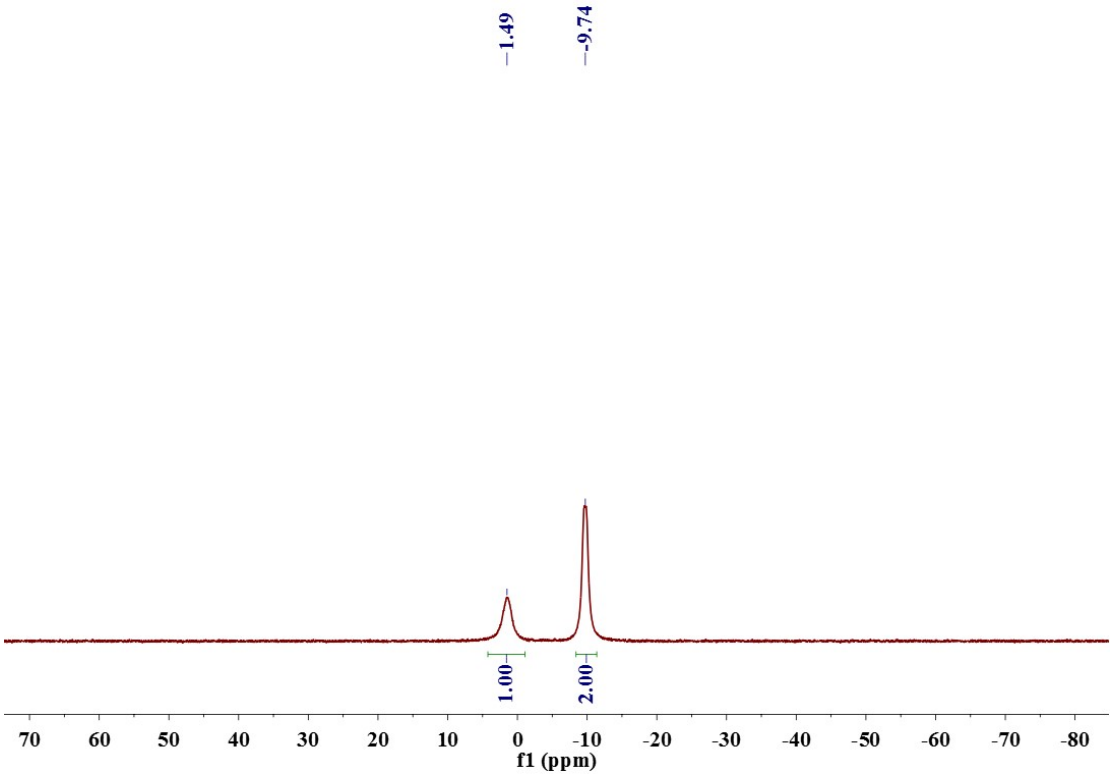

Figure S5. ^{31}P NMR spectrum of **1** in $CDCl_3$.

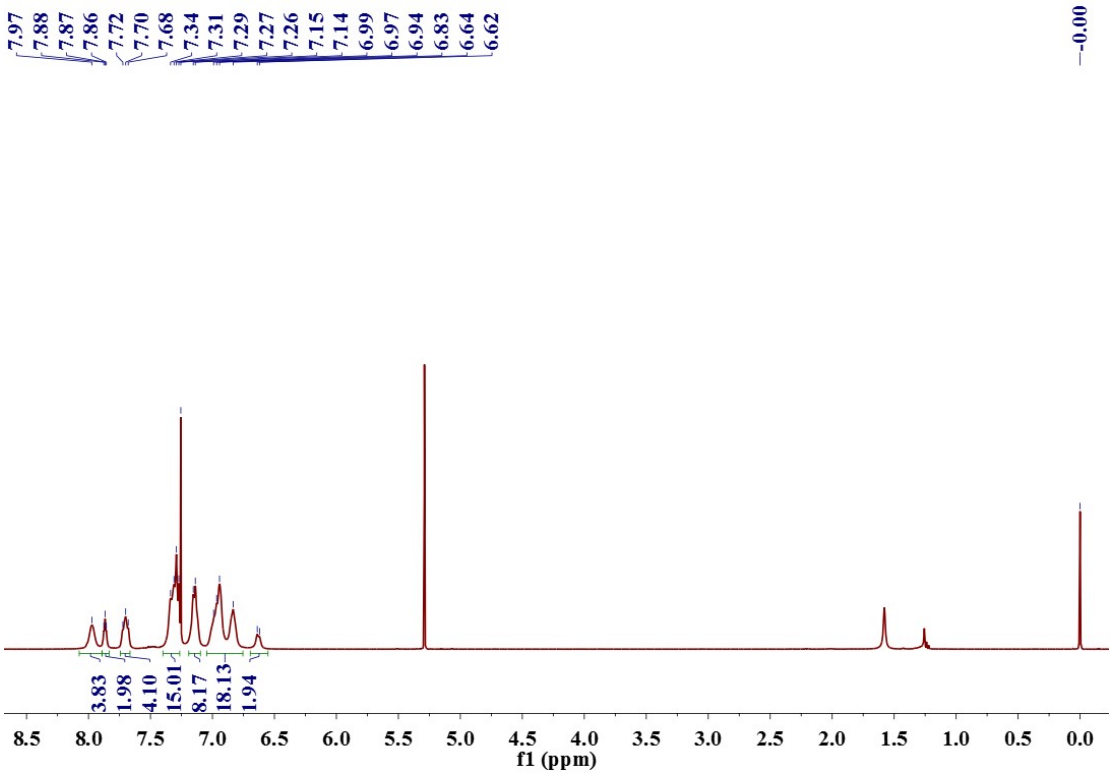

Figure S6. ^{1}H NMR spectrum of **2** in $CDCl_3$.

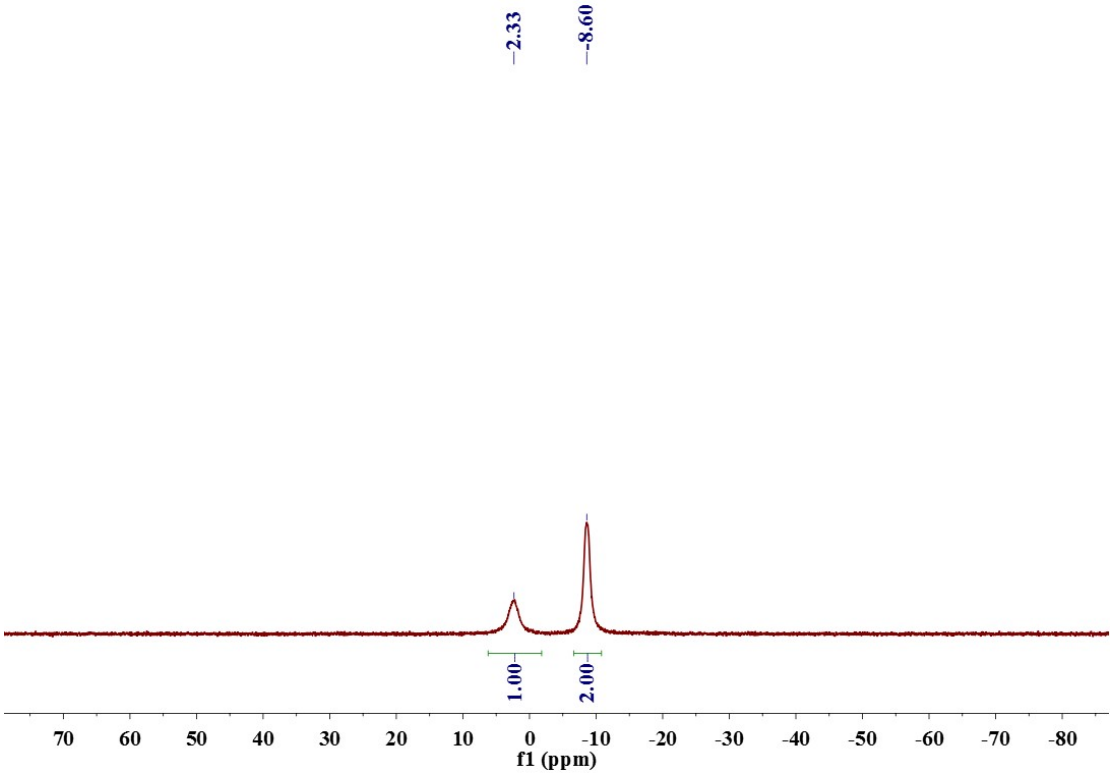

Figure S7. ^{31}P NMR spectrum of **2** in $CDCl_3$.

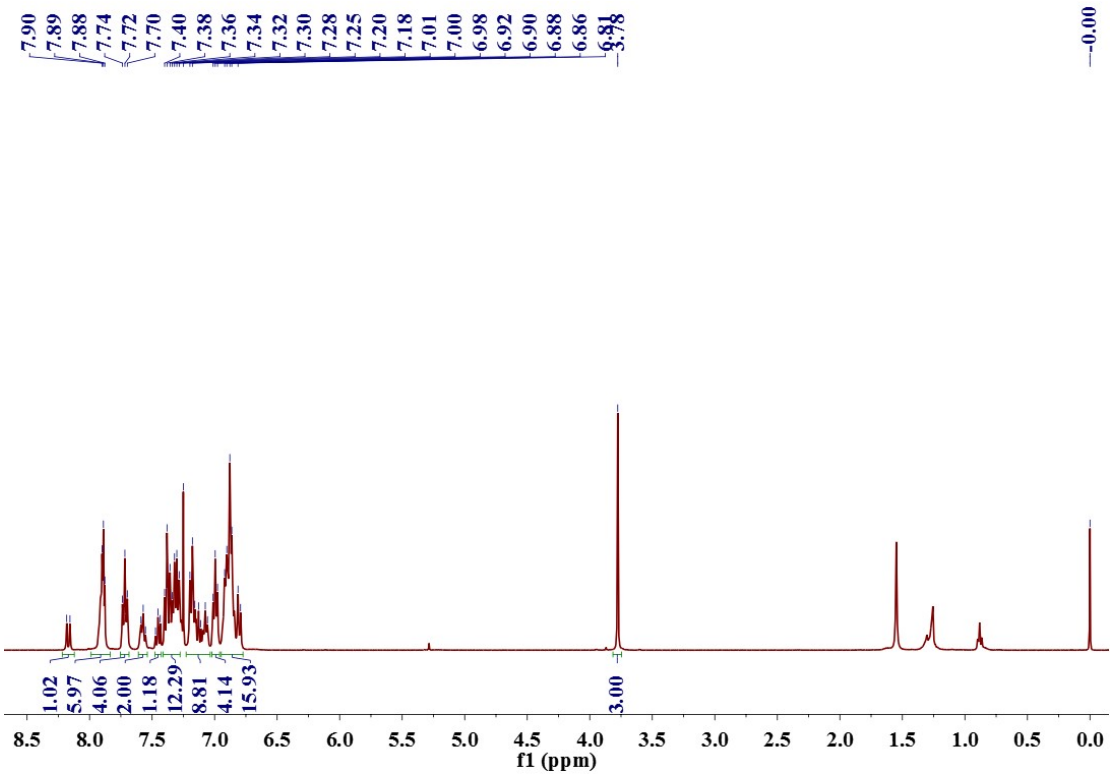

Figure S8. ^{1}H NMR spectrum of **3** in $CDCl_3$.

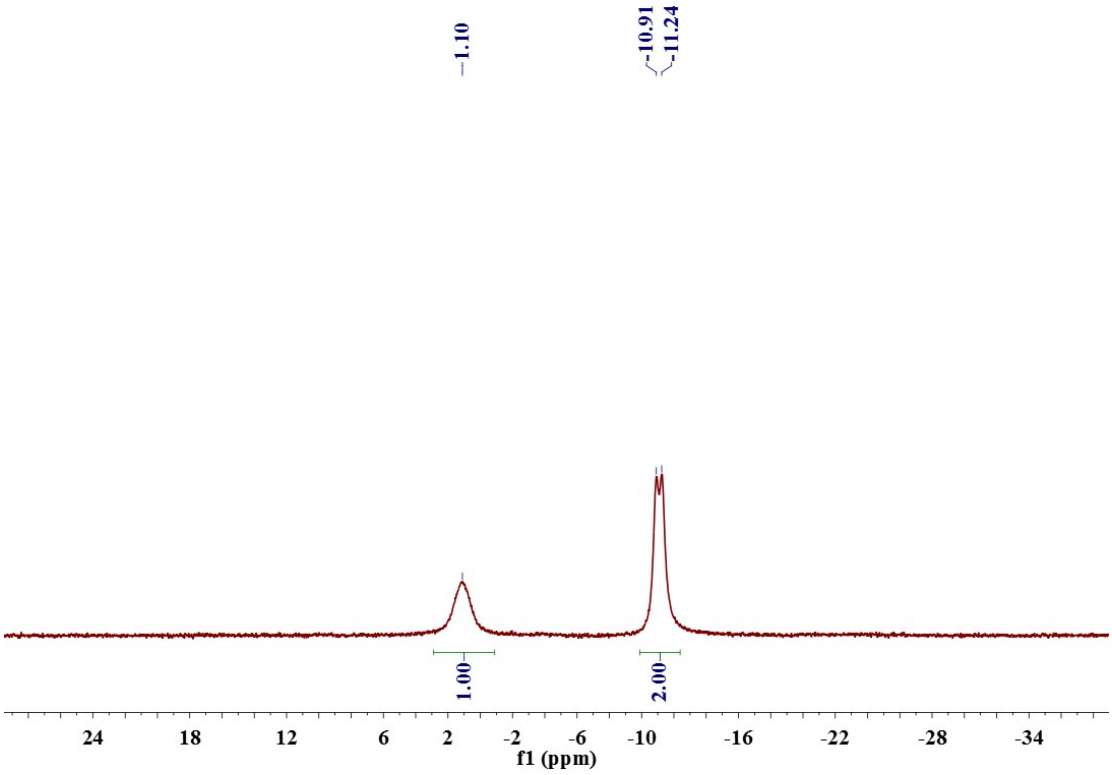

Figure S9. ^{31}P NMR spectrum of **3** in $CDCl_3$.

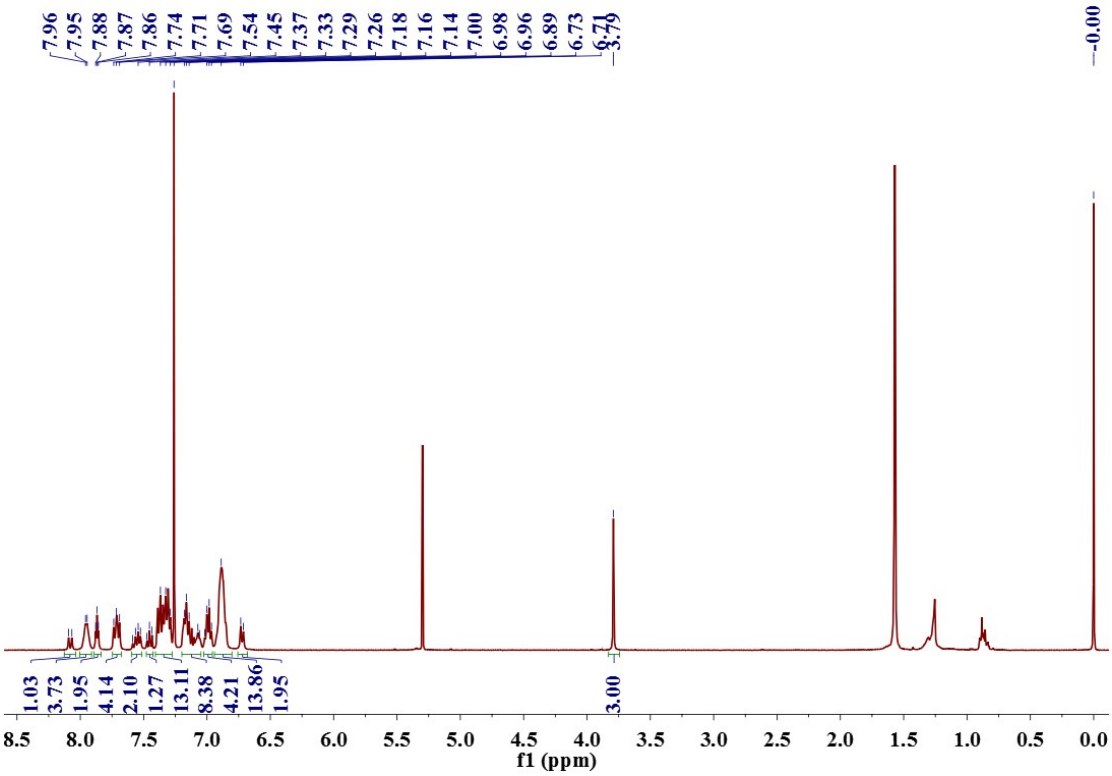

Figure S10. ^{1}H NMR spectrum of **4** in $CDCl_3$.

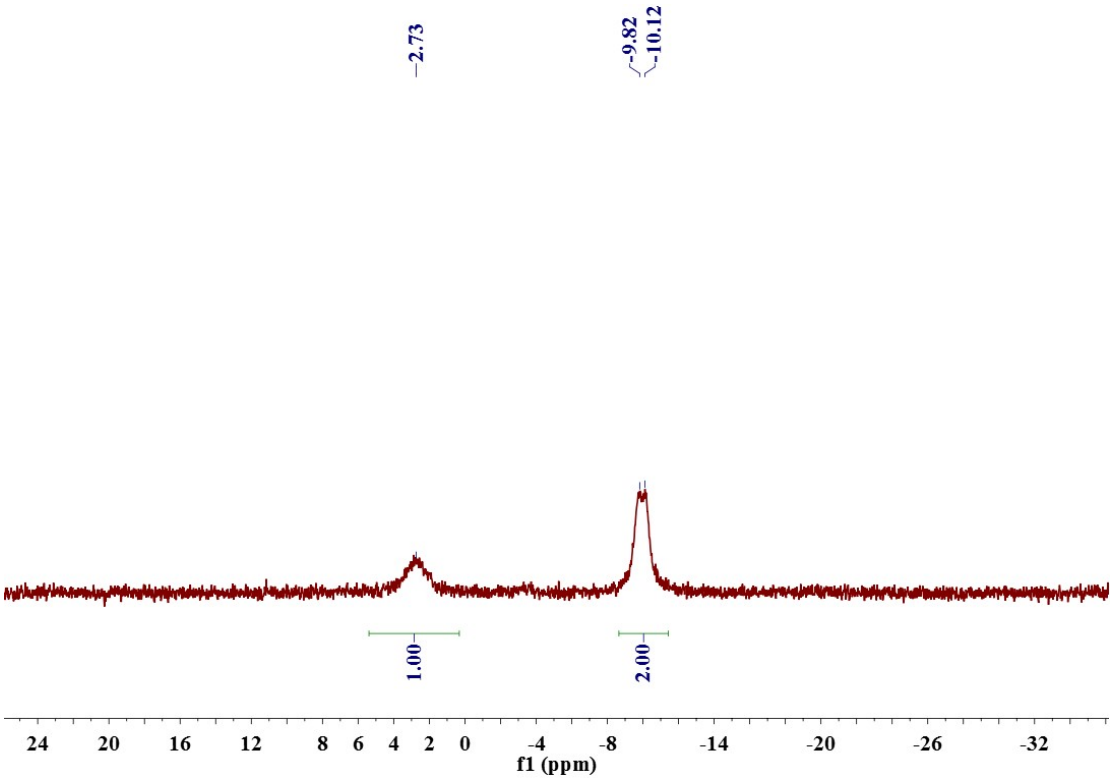

Figure S11. ^{31}P NMR spectrum of **4** in $CDCl_3$.

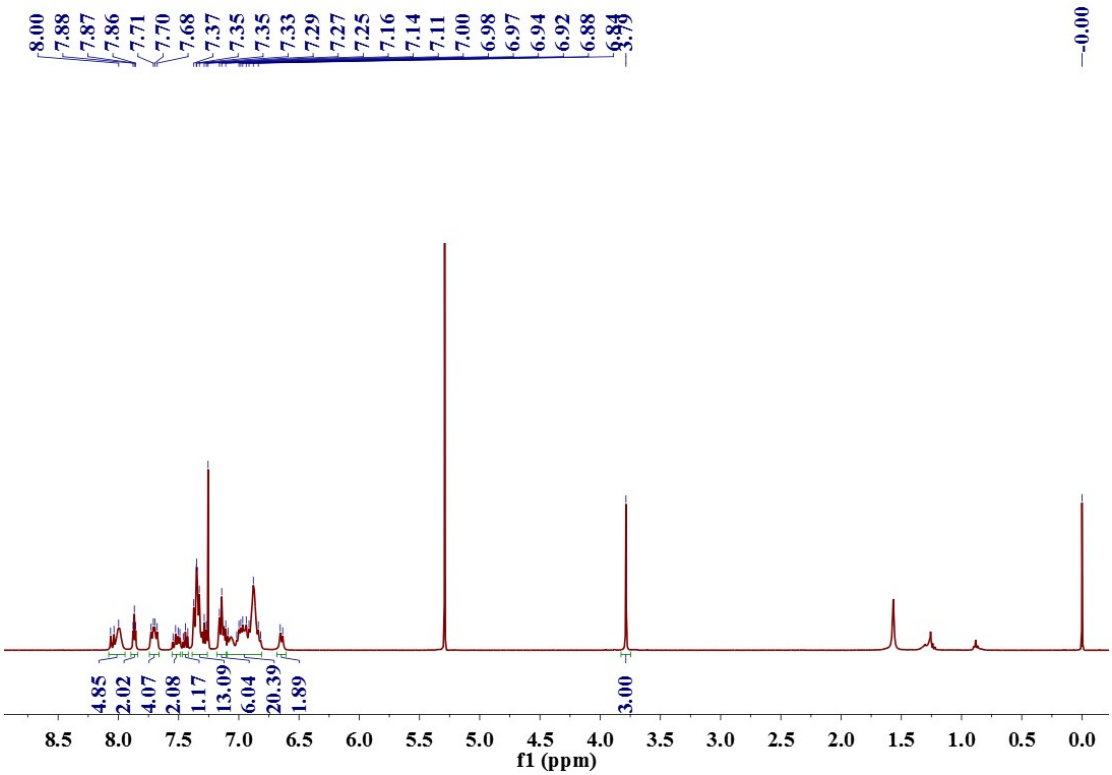

Figure S12. ^{1}H NMR spectrum of **5** in $CDCl_3$.

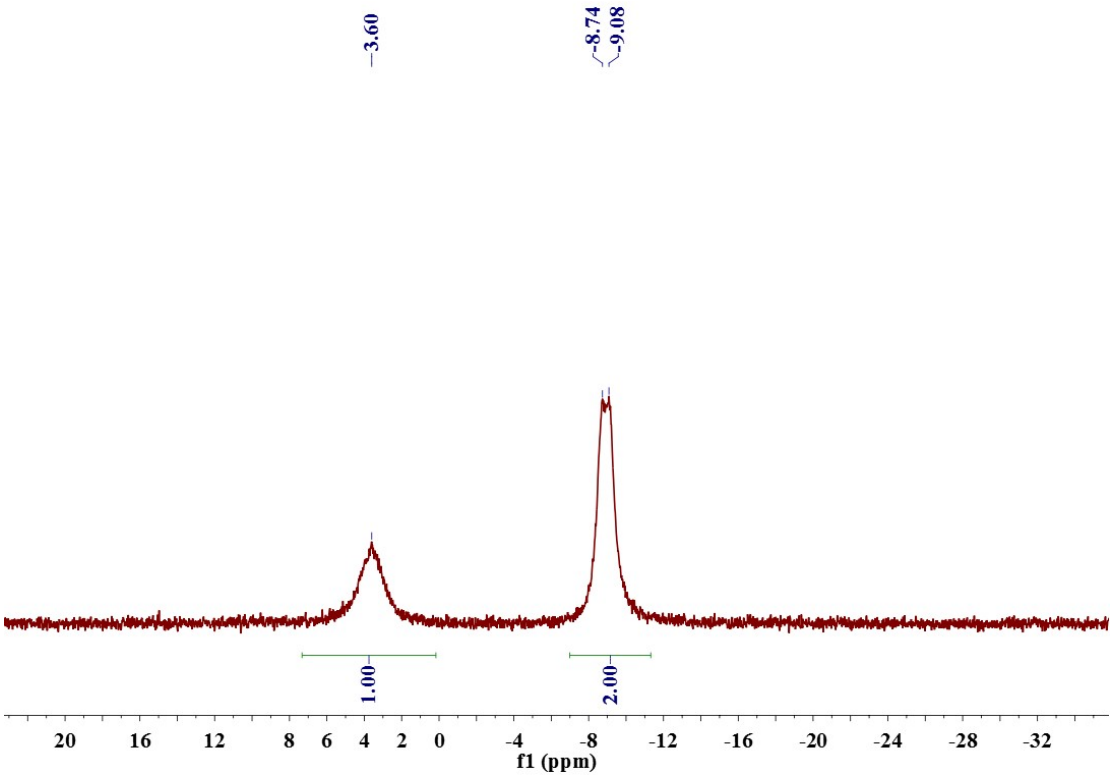

Figure S13. ^{31}P NMR spectrum of **5** in $CDCl_3$.

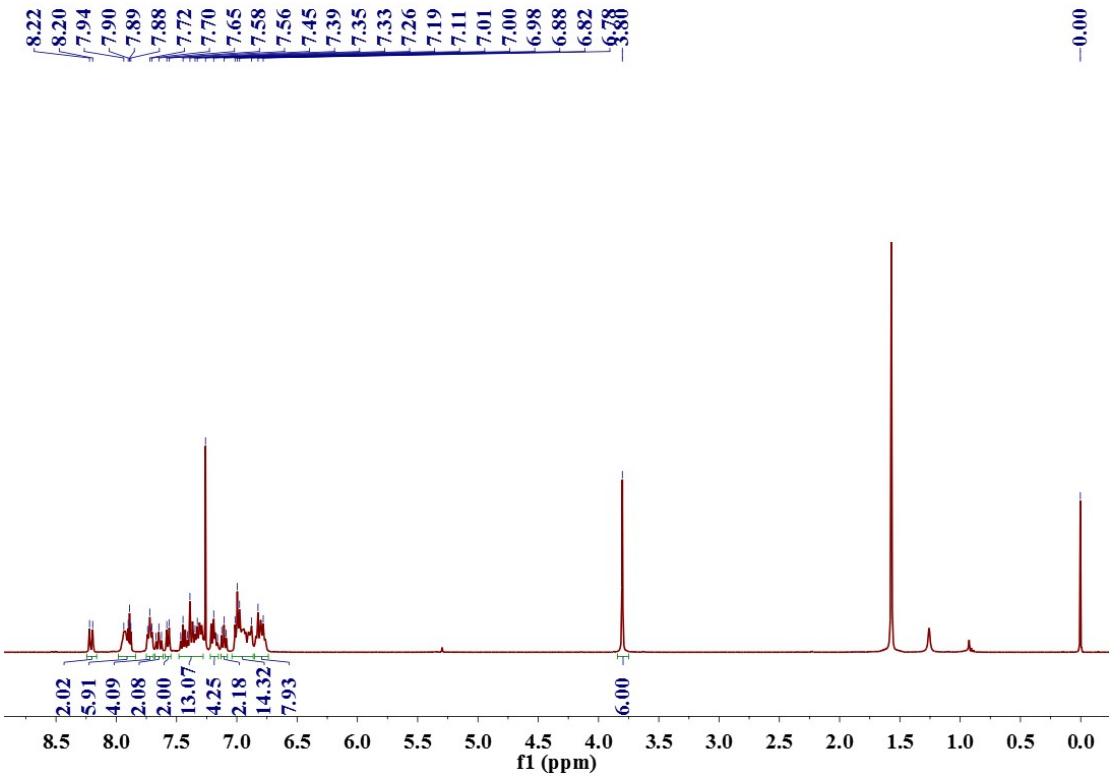

Figure S14. ^{1}H NMR spectrum of **6** in $CDCl_3$.

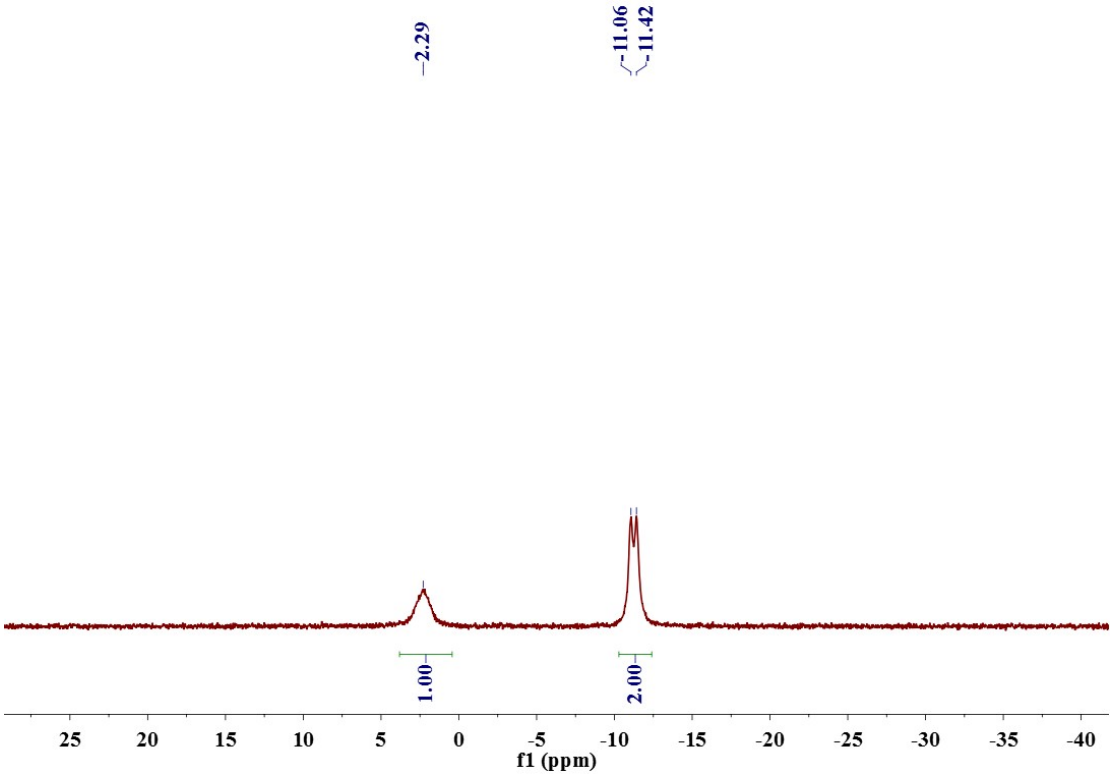

Figure S15. ^{31}P NMR spectrum of **6** in $CDCl_3$.

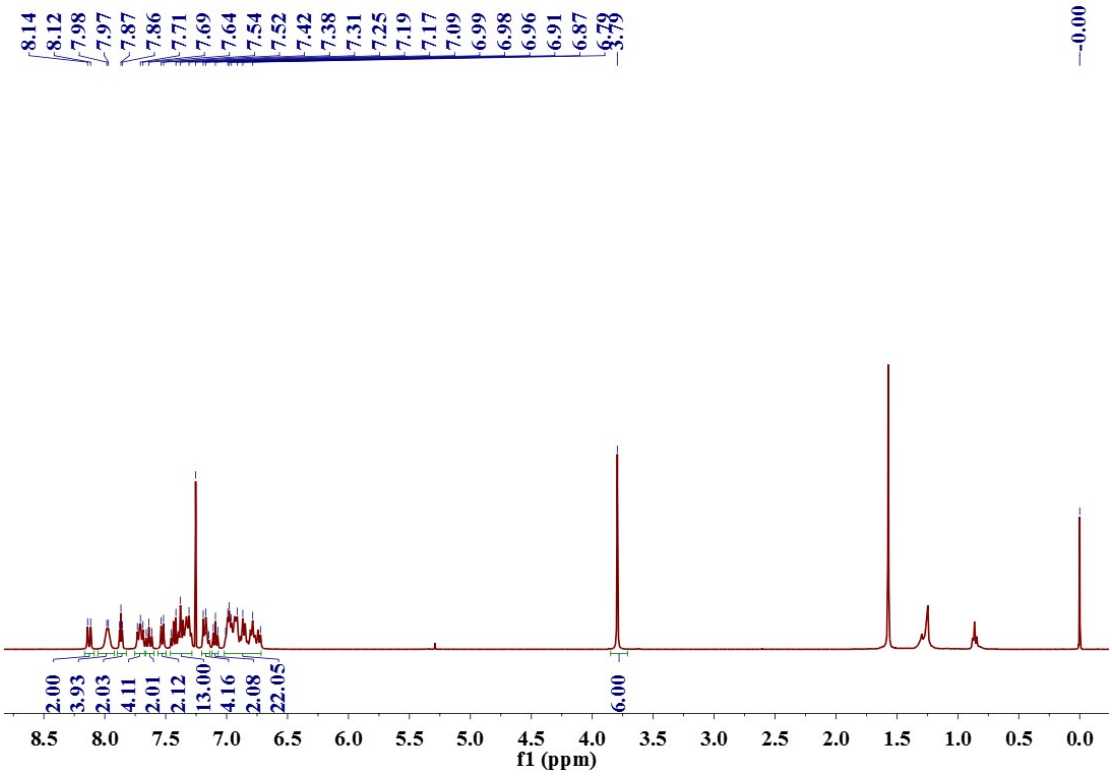

Figure S16. ^{1}H NMR spectrum of **7** in $CDCl_3$.

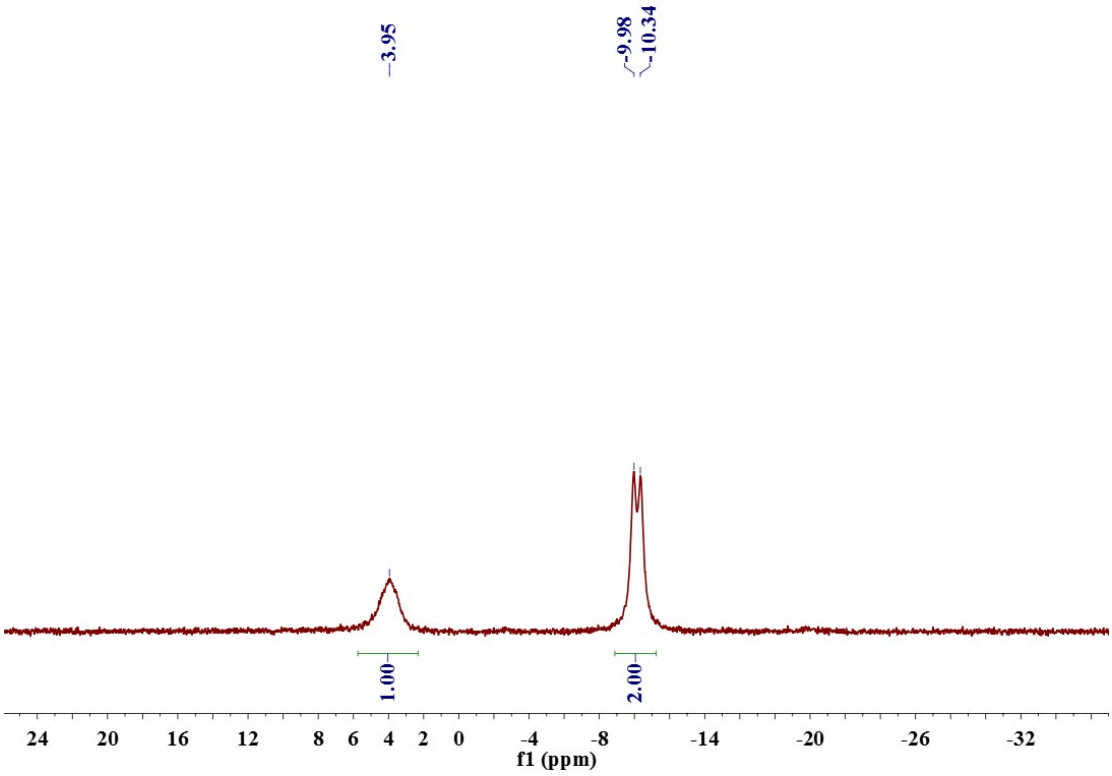

Figure S17. ^{31}P NMR spectrum of **7** in $CDCl_3$.

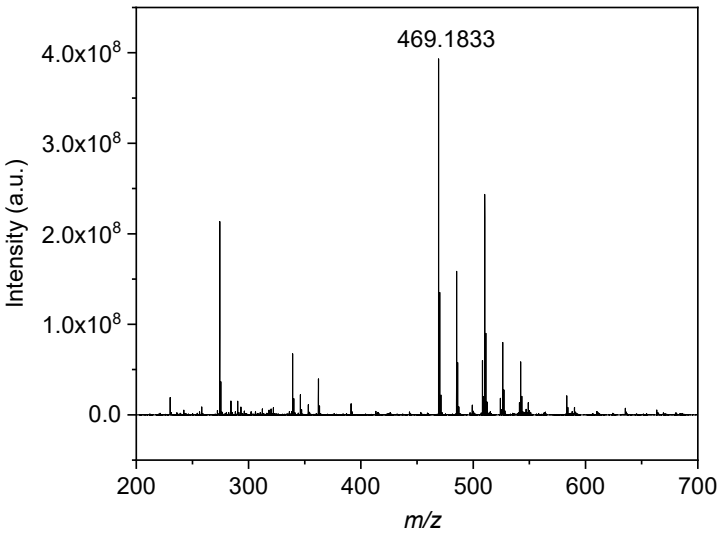

Figure S18. Mass spectrum of **DCzP**.

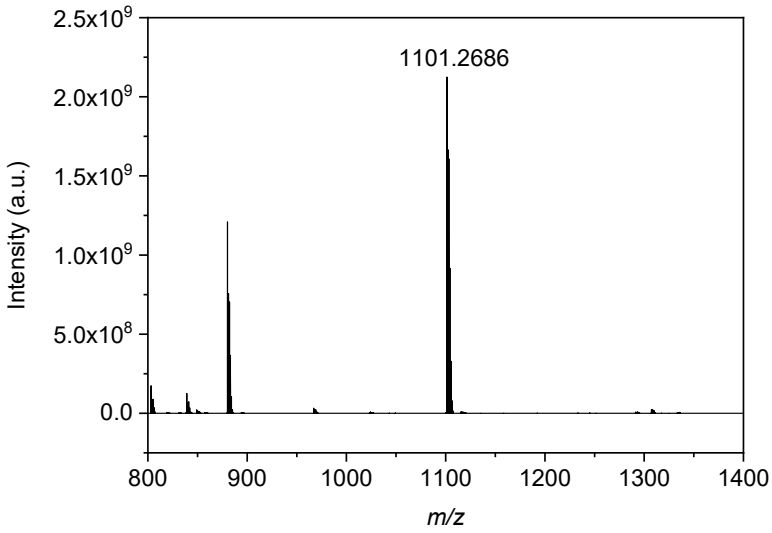

Figure S19. Mass spectrum of **1**.

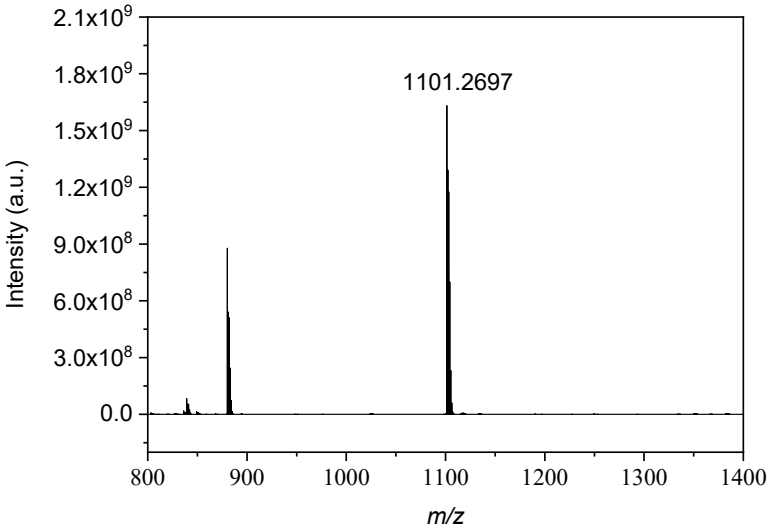

Figure S20. Mass spectrum of **2**.

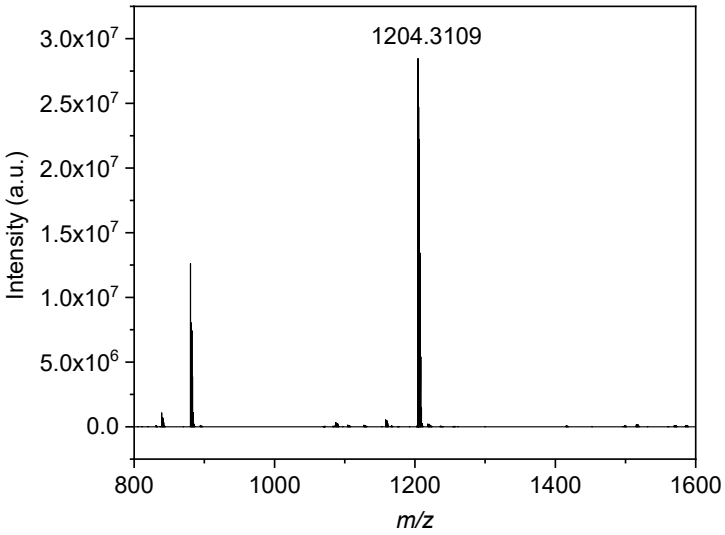

Figure S21. Mass spectrum of 3.

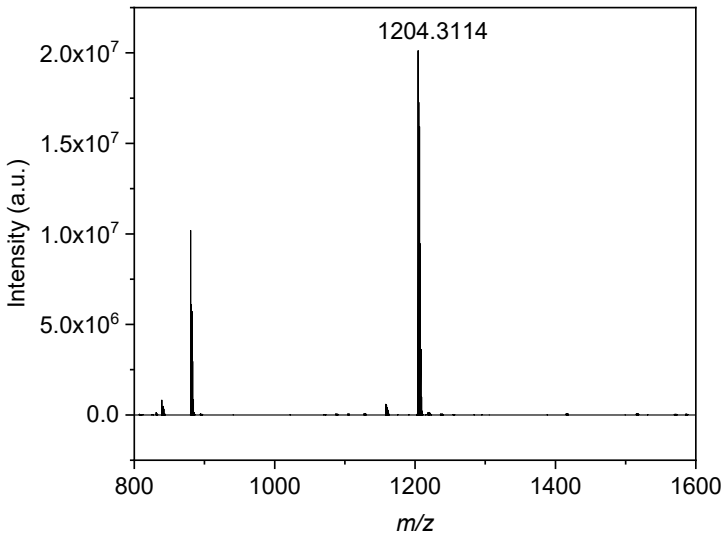

Figure S22. Mass spectrum of **4**.

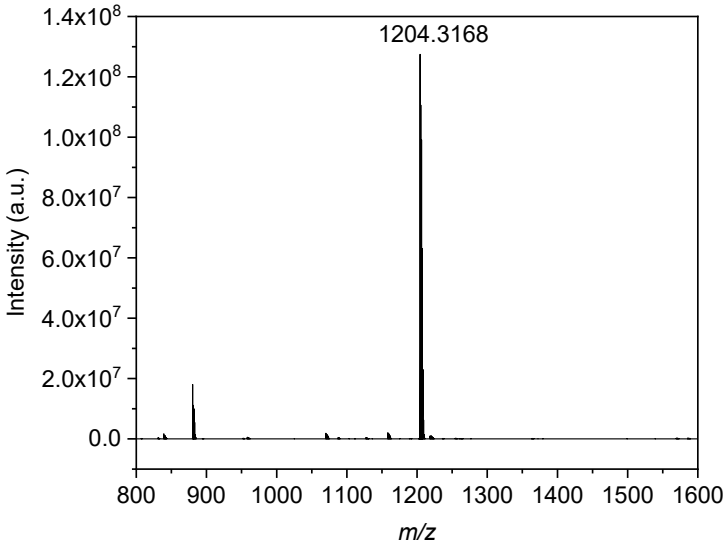

Figure S23. Mass spectrum of **5**.

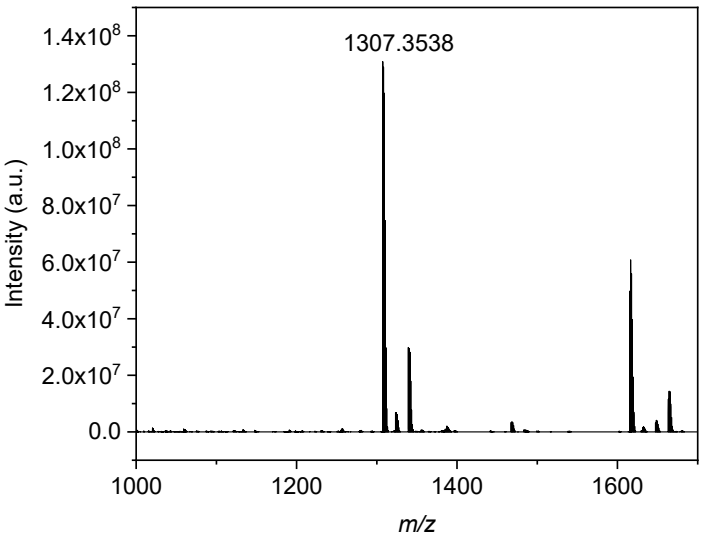

Figure S24. Mass spectrum of **6**.

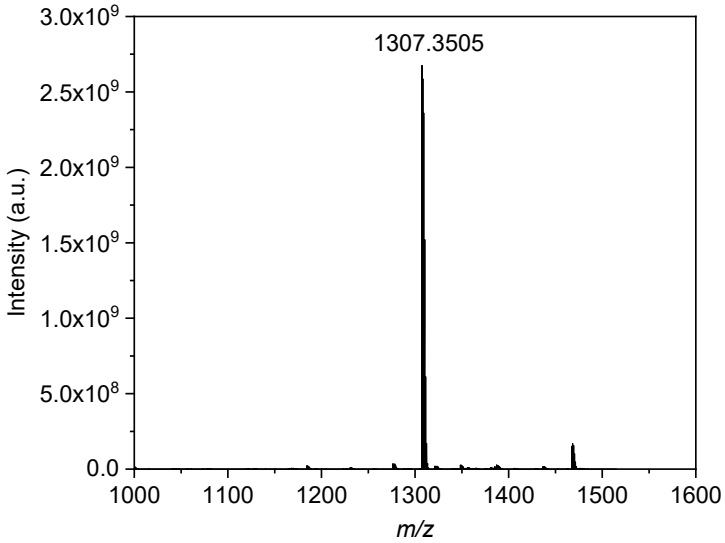

Figure S25. Mass spectrum of **7**.

3. Molecular structures

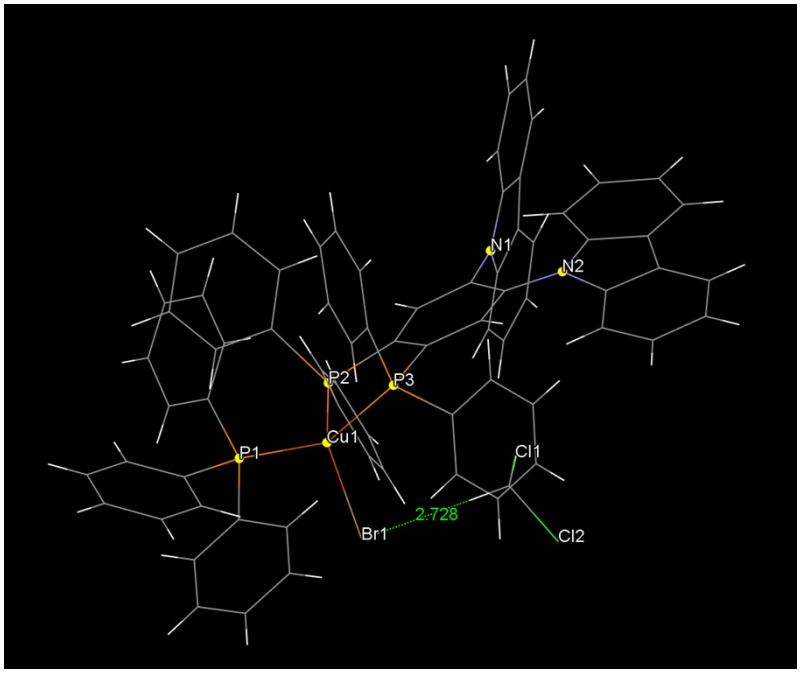

Figure S26. Intermolecular Br···H (CH_2Cl_2) interaction in **1**.

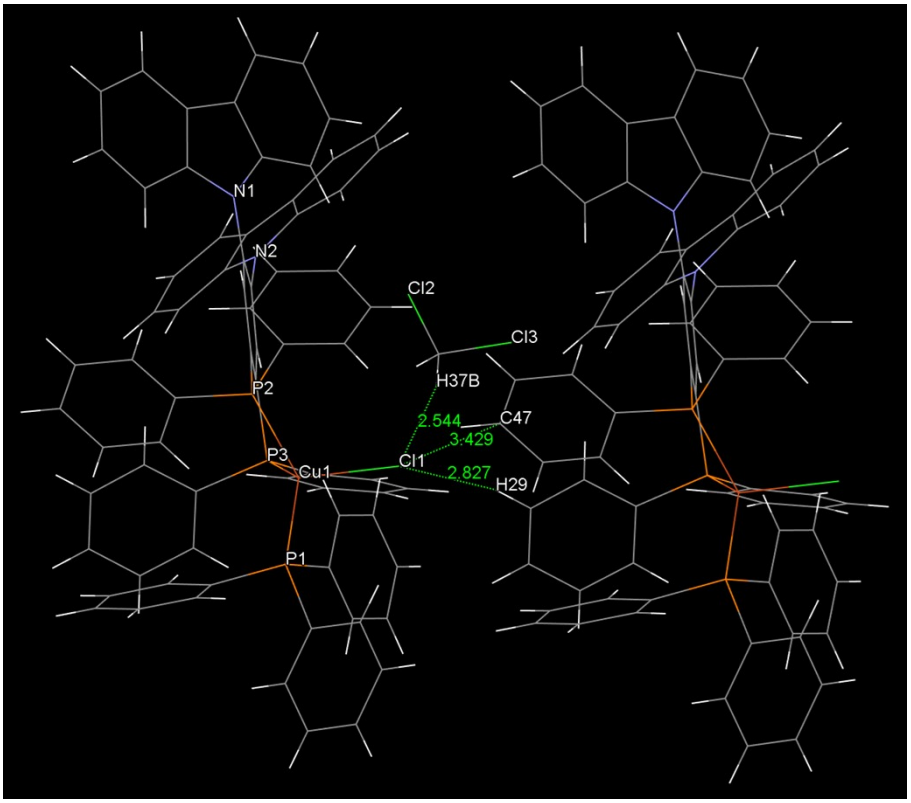

Figure S27. Intermolecular Cl···H (CH_2Cl_2), Cl···H (phenyl) and Cl ···C (phenyl) interactions in **2**.

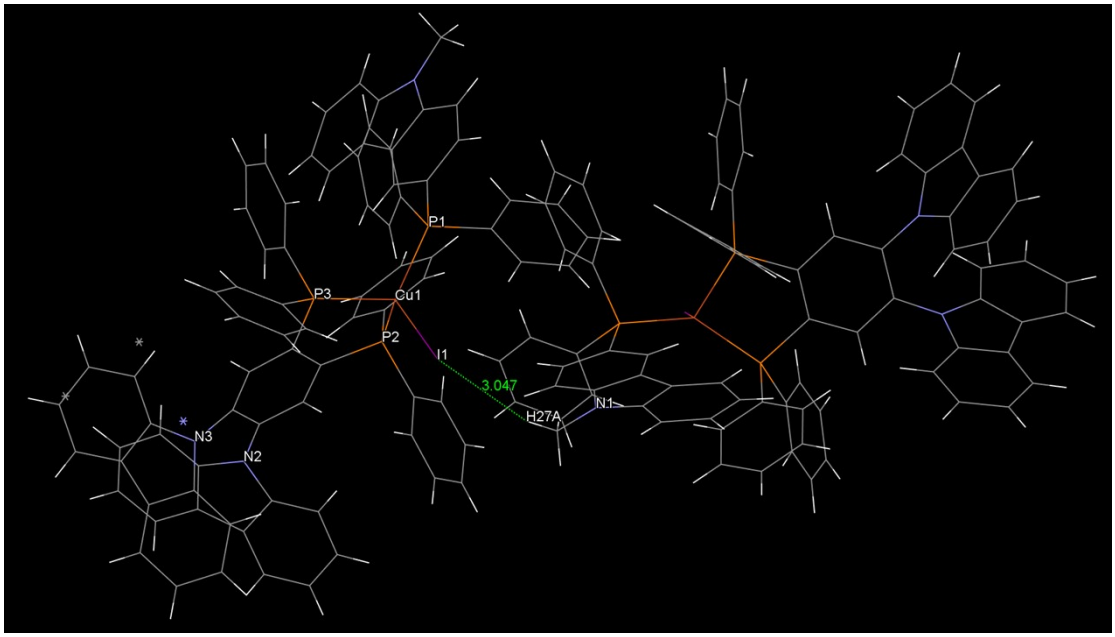

Figure S28. Intermolecular I···H (CH_3) interaction in **3**.

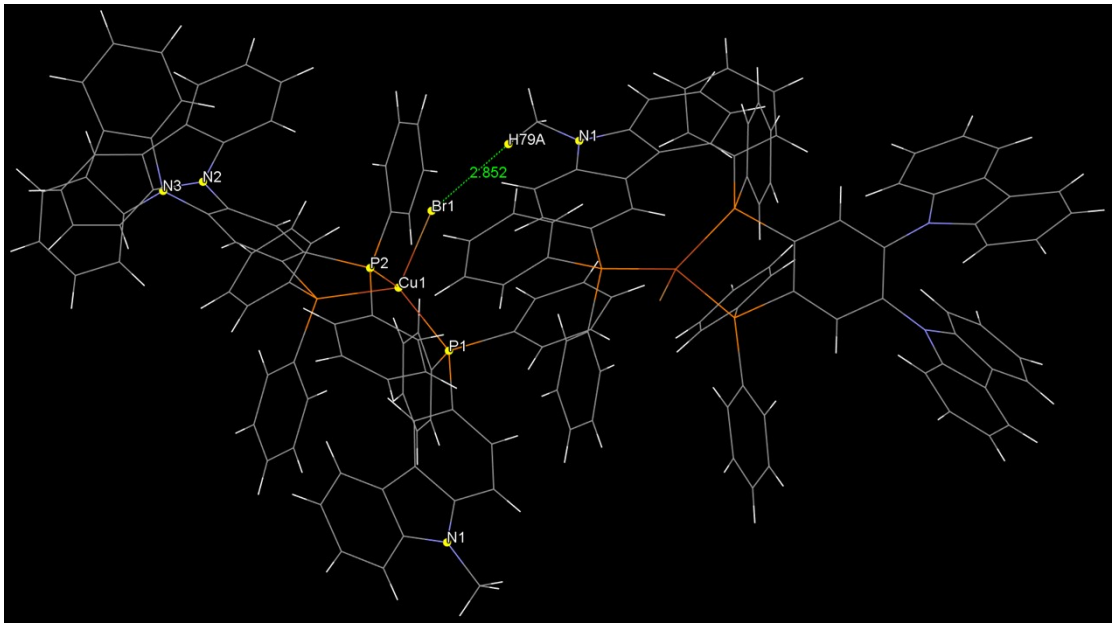

Figure S29. Intermolecular Br···H (CH_3) interaction in **4**.

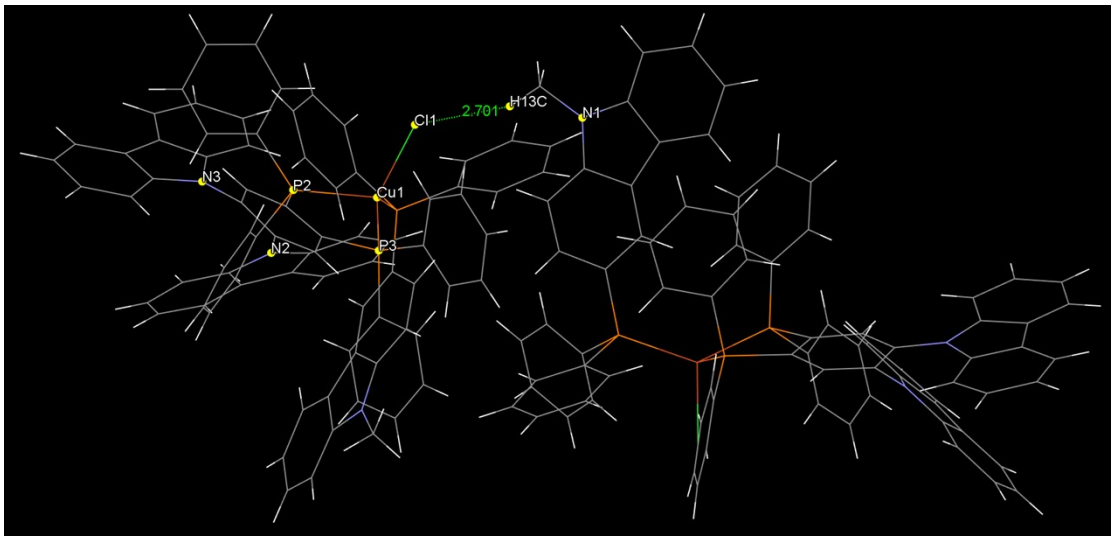

Figure S30. Intermolecular Cl···H (CH_3) interaction in **5**.

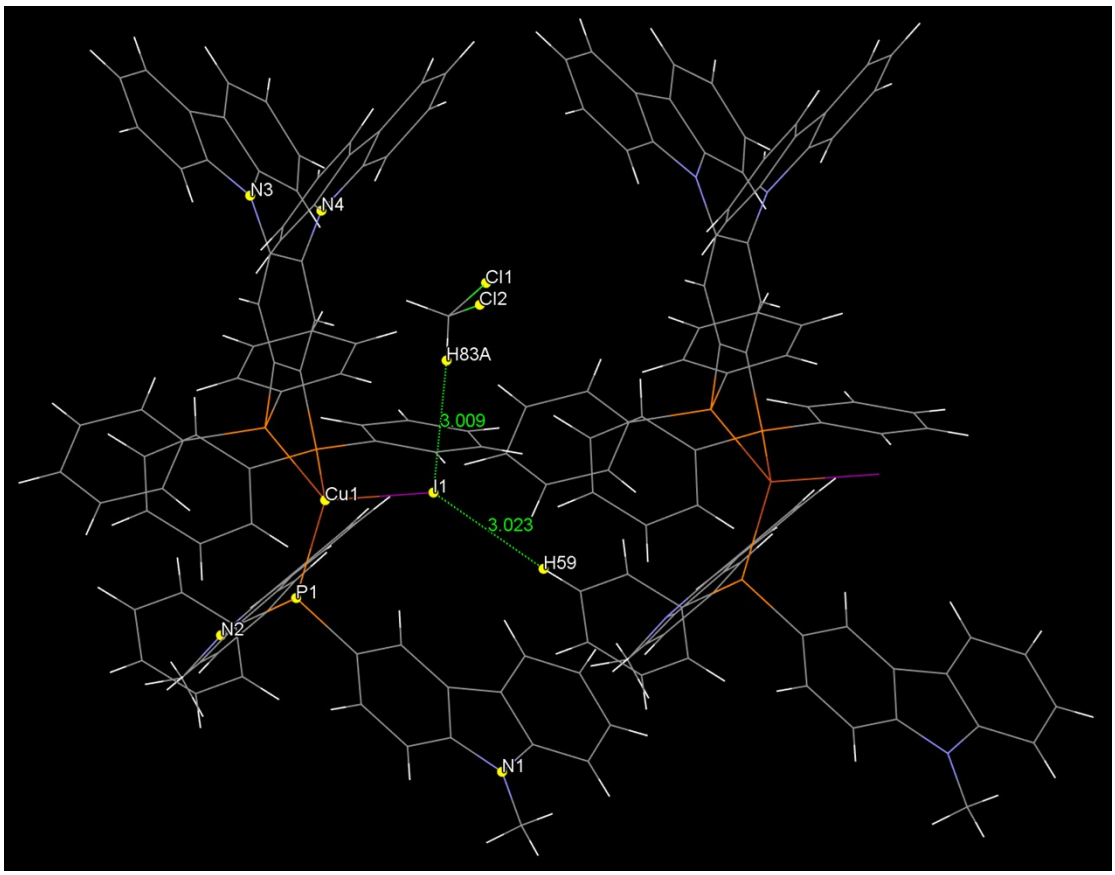

Figure S31. Intermolecular I···H (phenyl), I ···H (CH_2Cl_2) interactions in **6**.

4. Photophysical properties

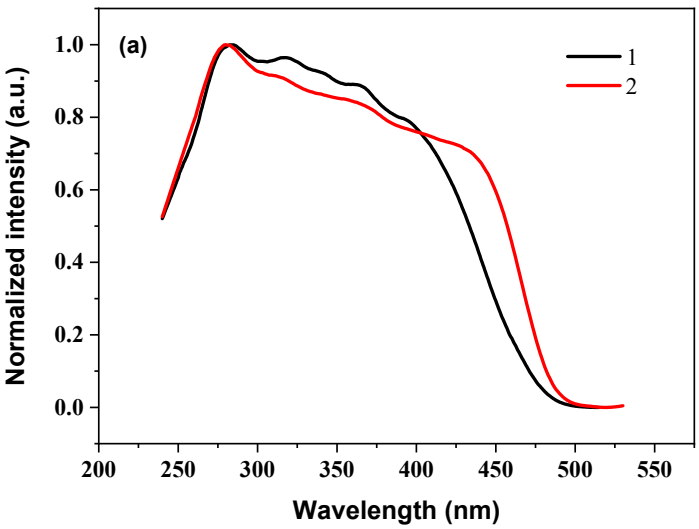

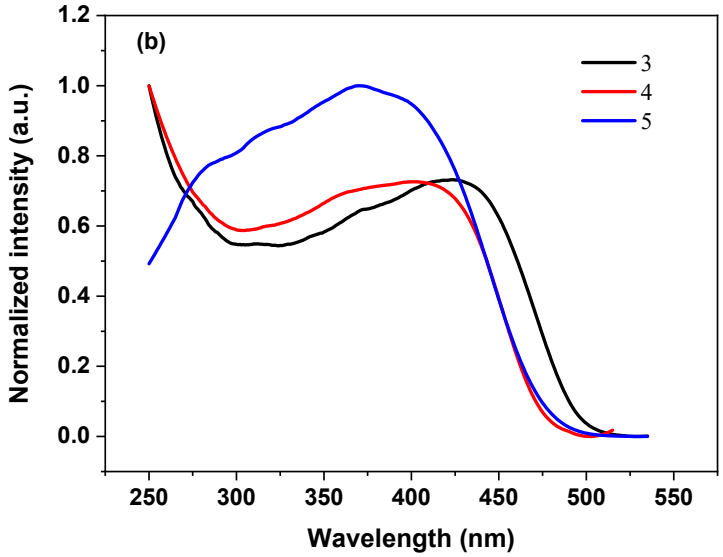

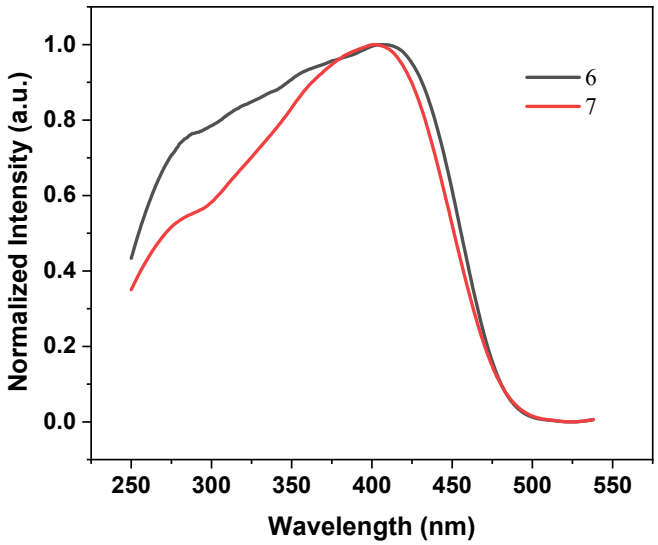

Figure S32. Normalized excitation spectra of **1–7** in powder at 297 K (λ_{em} = 531 nm for **1**, λ_{em} = 555 nm for **2**, λ_{em} = 560 nm for **3**, λ_{em} = 535 nm for **4**, λ_{em} = 558 nm for **5**, λ_{em} = 556 nm for **6**, λ_{em} = 557 nm for **7**).

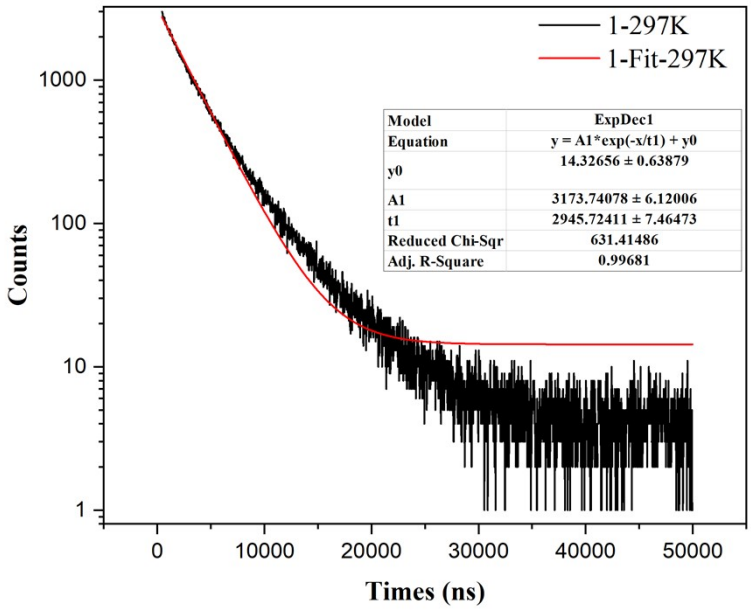

Figure 33. Time profiles of luminescence decay and exponential fit spectrum of **1** at 297 K (λ_{em} = 531 nm).

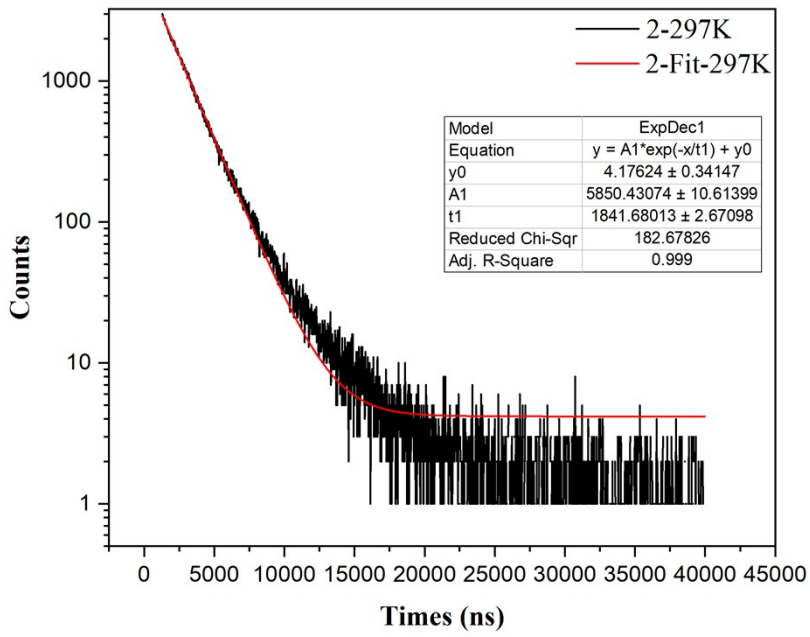

Figure S34. Time profiles of luminescence decay and exponential fit spectrum of **2** at 297 K (λ_{em} = 553 nm).

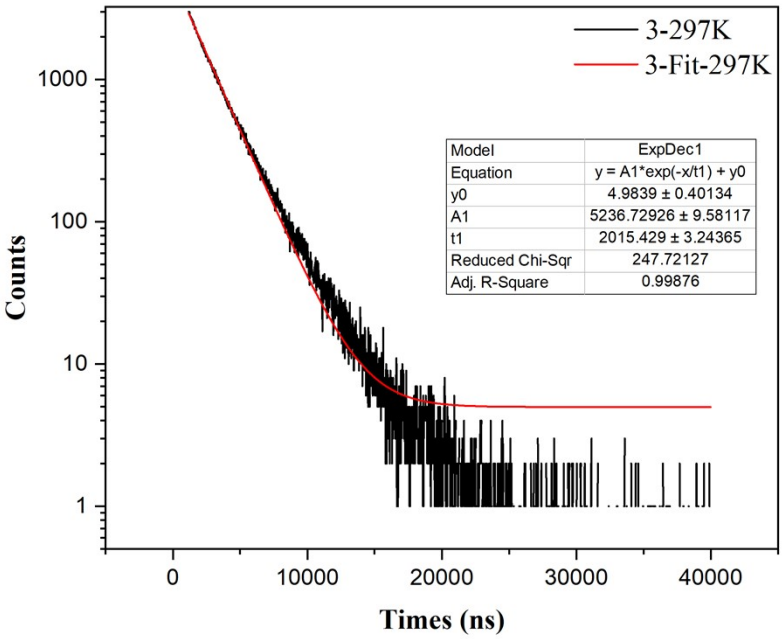

Figure S35. Time profiles of luminescence decay and exponential fit spectrum of **3** at 297 K (λ_{em} = 555 nm).

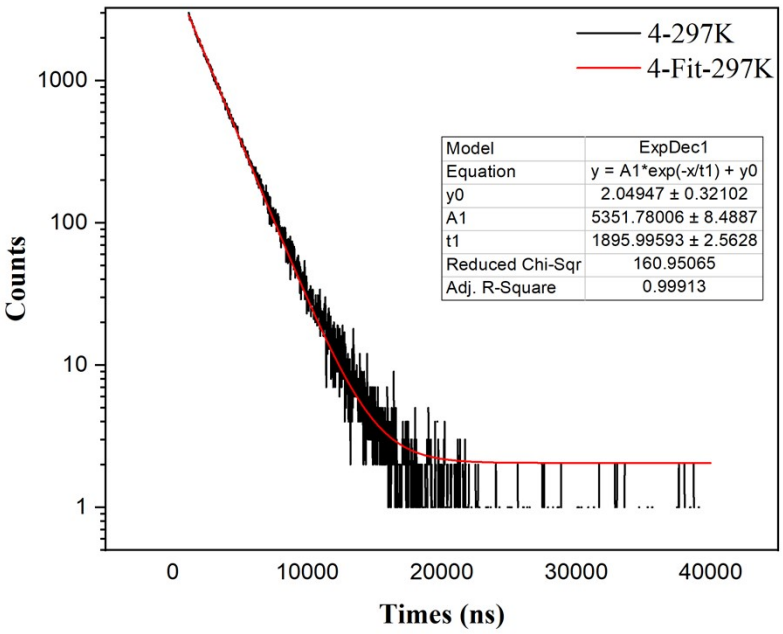

Figure S36. Time profiles of luminescence decay and exponential fit spectrum of **4** at 297 K (λ_{em} = 534 nm).

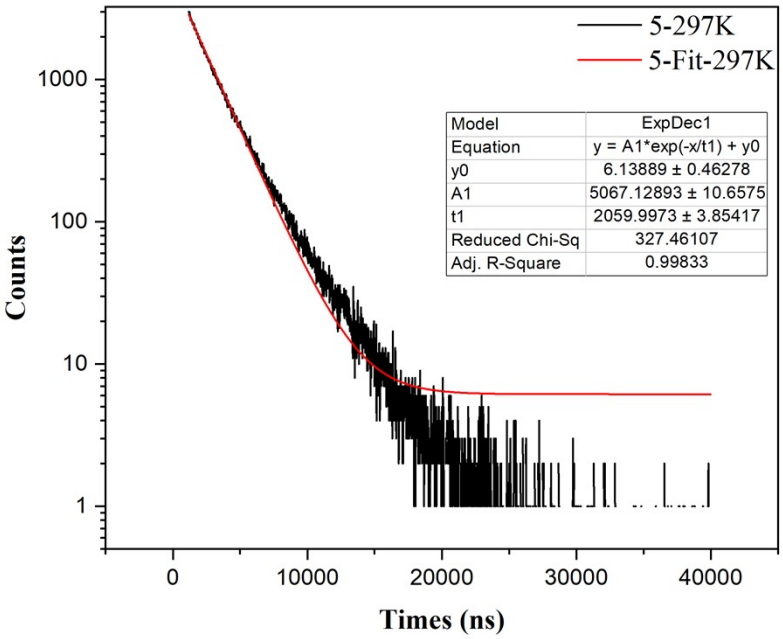

Figure S37. Time profiles of luminescence decay and exponential fit spectrum of **5** at 297 K (λ_{em} = 557 nm).

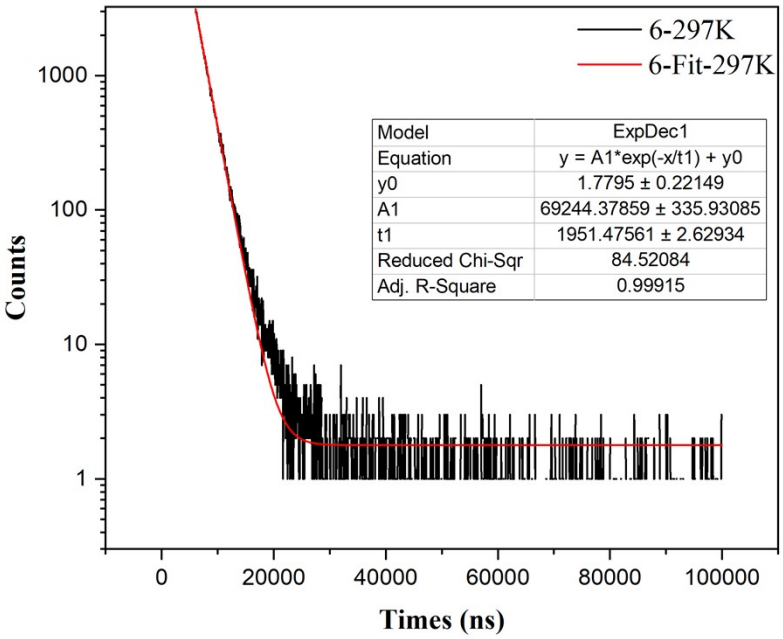

Figure S38. Time profiles of luminescence decay and exponential fit spectrum of **6** at 297 K (λ_{em} = 556 nm).

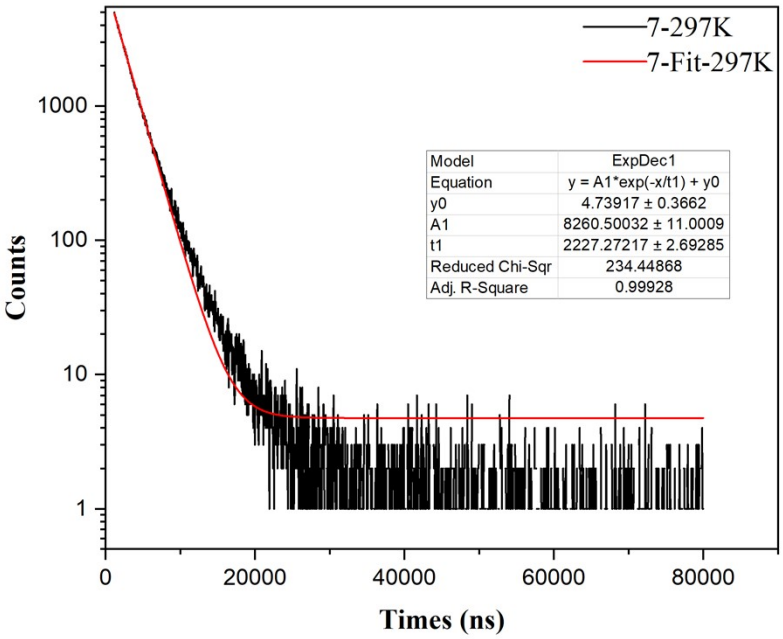

Figure S39. Time profiles of luminescence decay and exponential fit spectrum of **7** at 297 K (λ_{em} = 558 nm).

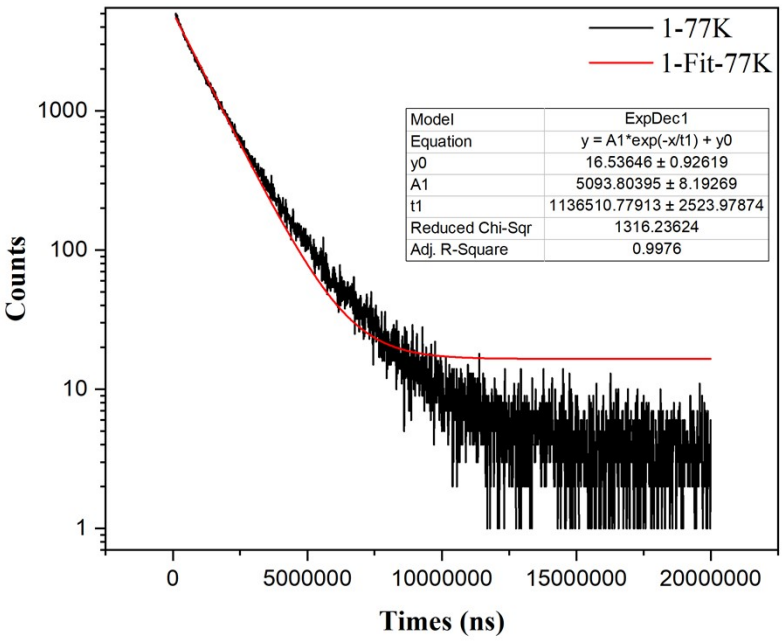

Figure S40. Time profiles of luminescence decay and exponential fit spectrum of **1** at 77 K (λ_{em} = 547 nm).

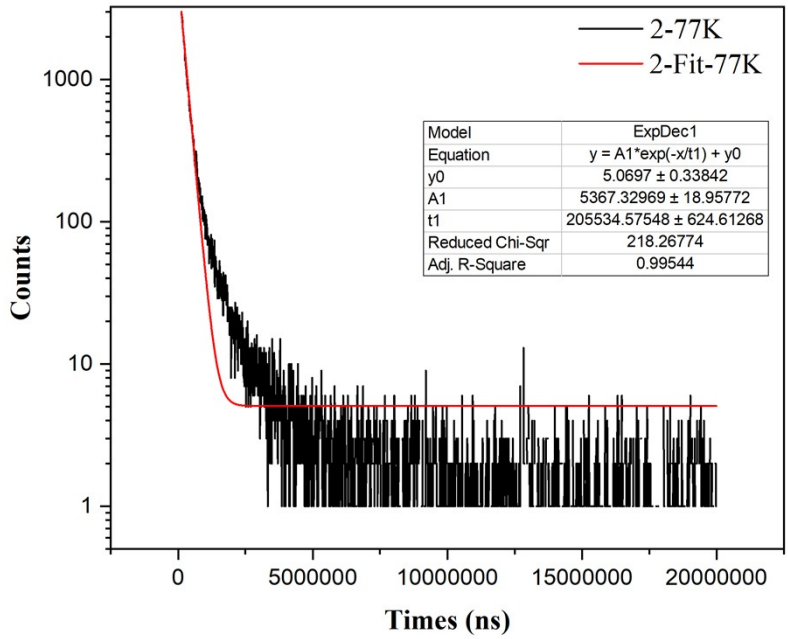

Figure S41. Time profiles of luminescence decay and exponential fit spectrum of **2** at 77 K (λ_{em} = 556 nm).

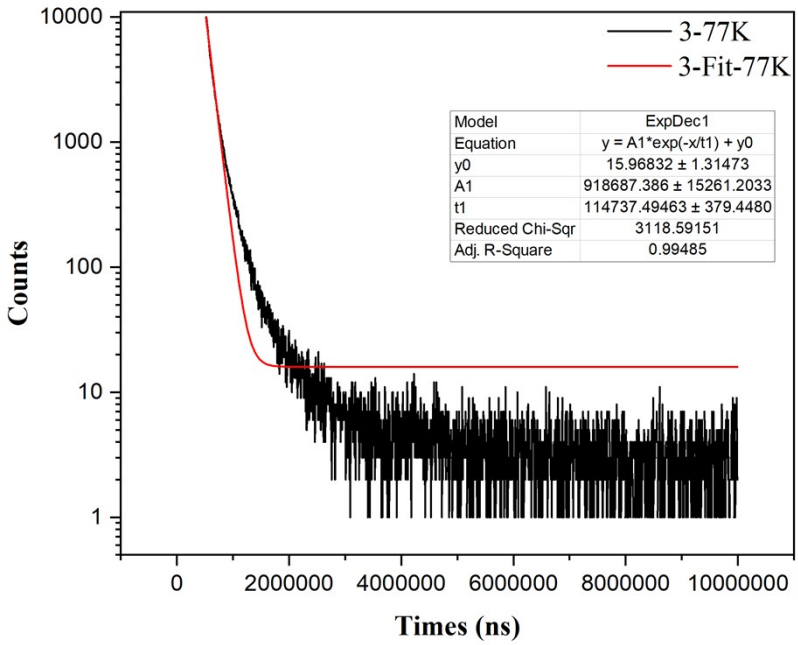

Figure S42. Time profiles of luminescence decay and exponential fit spectrum of **3** at 77 K (λ_{em} = 547 nm).

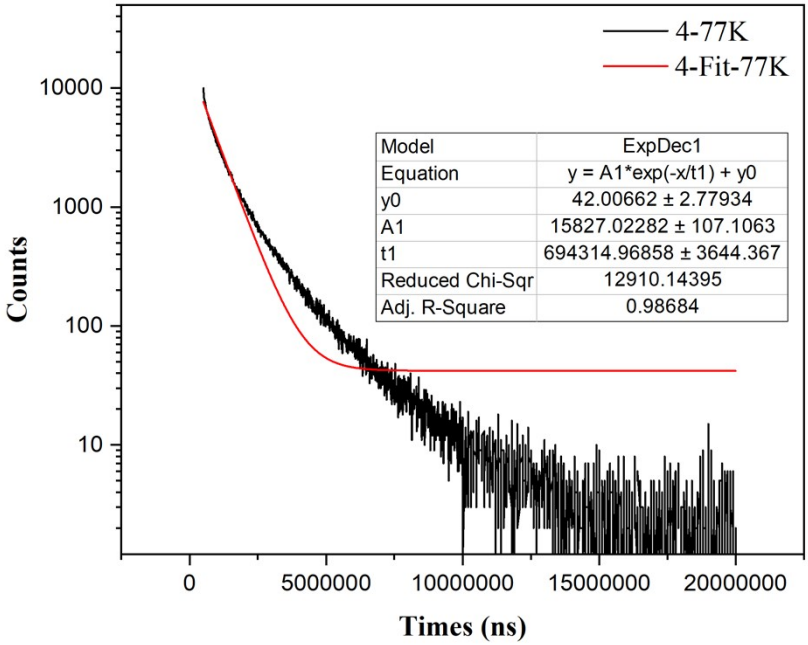

Figure S43. Time profiles of luminescence decay and exponential fit spectrum of **4** at 77 K (λ_{em} = 525 nm).

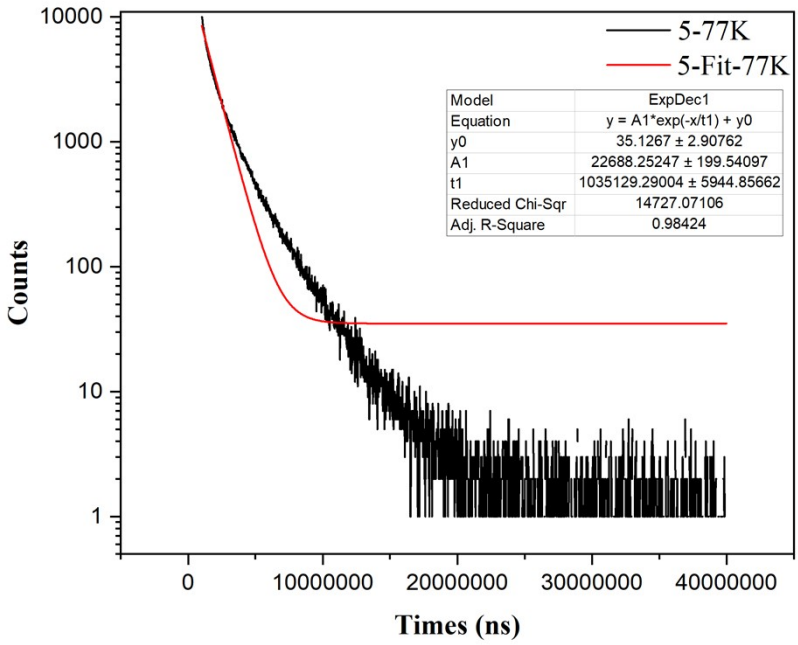

Figure S44. Time profiles of luminescence decay and exponential fit spectrum of **5** at 77 K (λ_{em} = 549 nm).

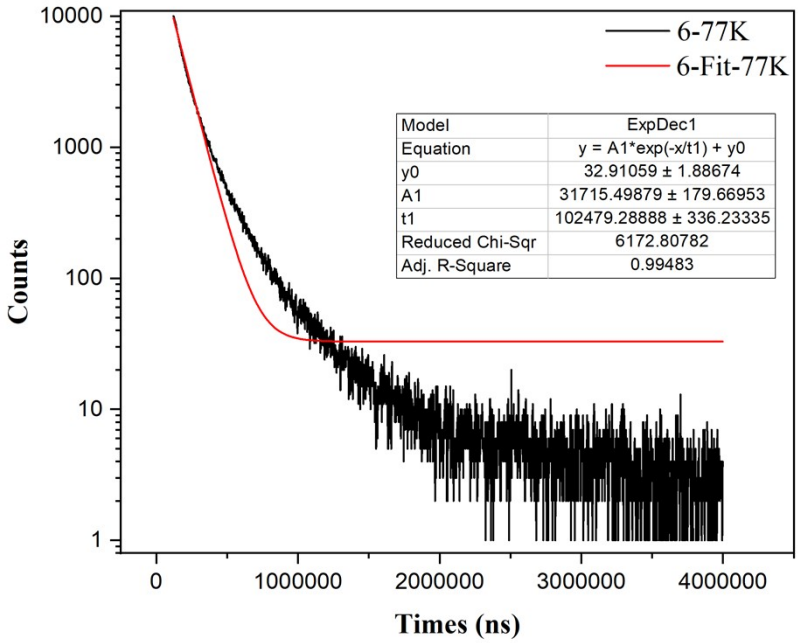

Figure S45. Time profiles of luminescence decay and exponential fit spectrum of **6** at 77 K (λ_{em} = 545 nm).

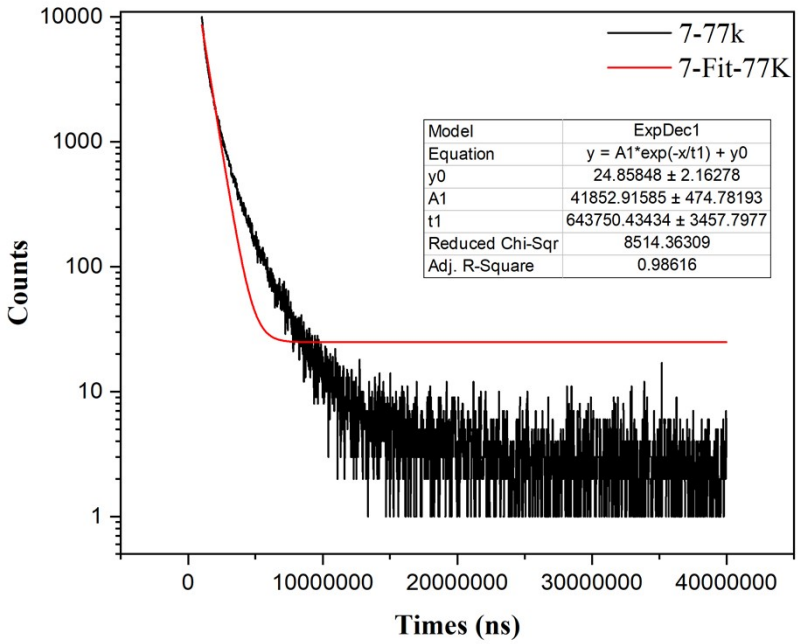

Figure S46. Time profiles of luminescence decay and exponential fit spectrum of **7** at 77 K (λ_{em} = 548 nm).

5. Computational details

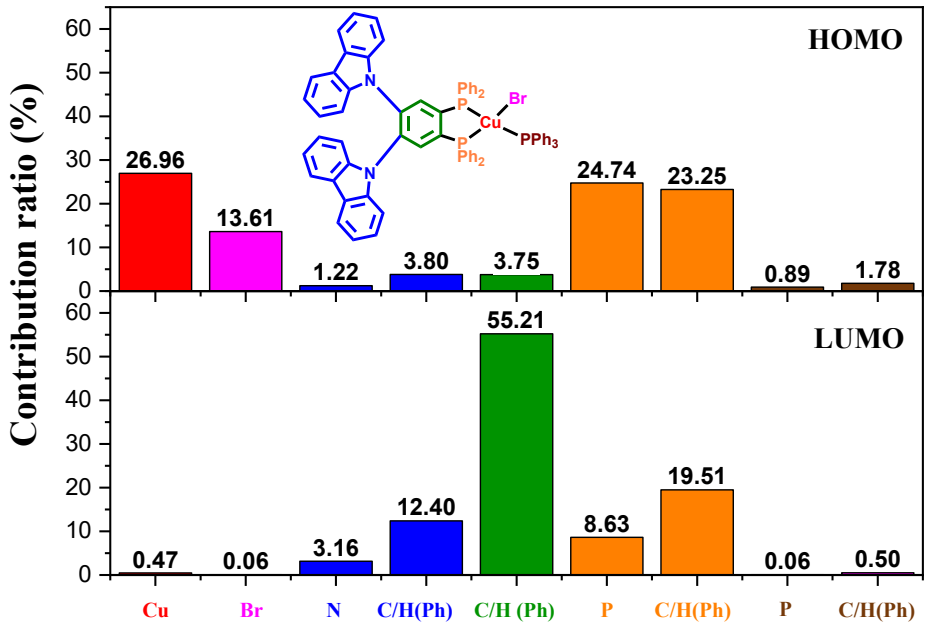

Figure S47. Compositions of the frontier molecular orbitals at optimized S_0 geometry of complex **1**.

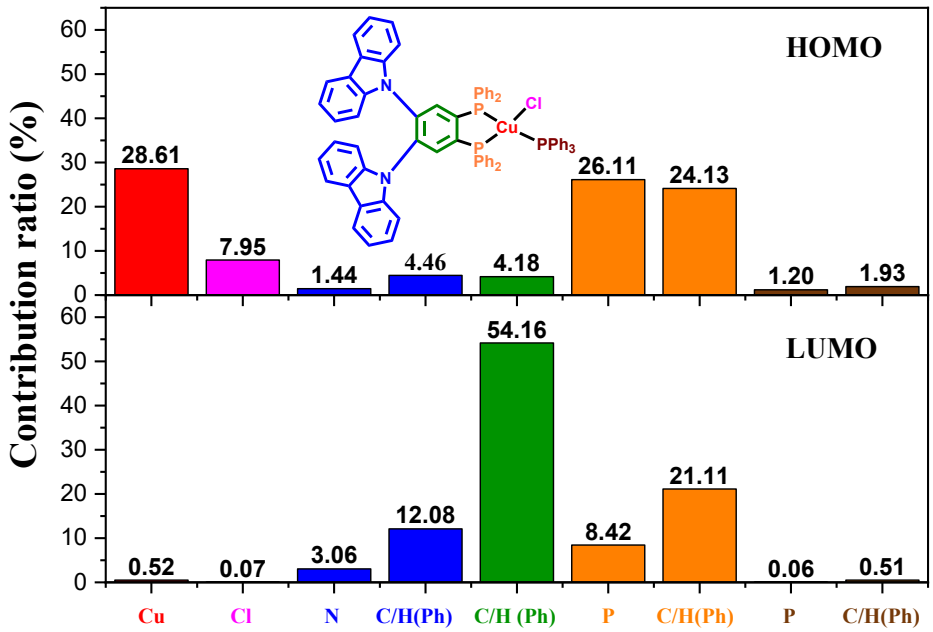

Figure S48. Compositions of the frontier molecular orbitals at optimized S_0 geometry of complex **2**.

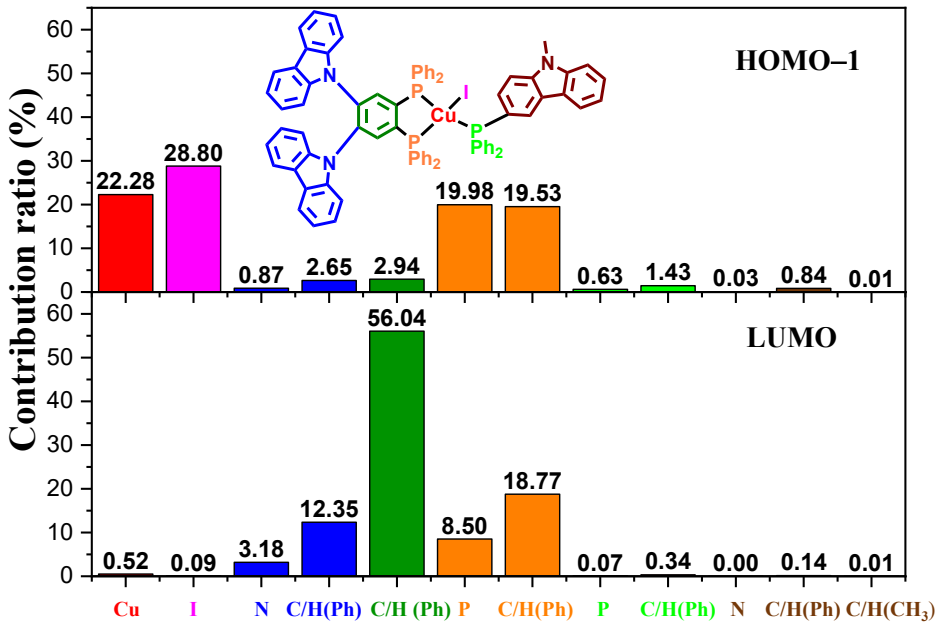

Figure S49. Compositions of the frontier molecular orbitals at optimized S_0 geometry of complex **3**.

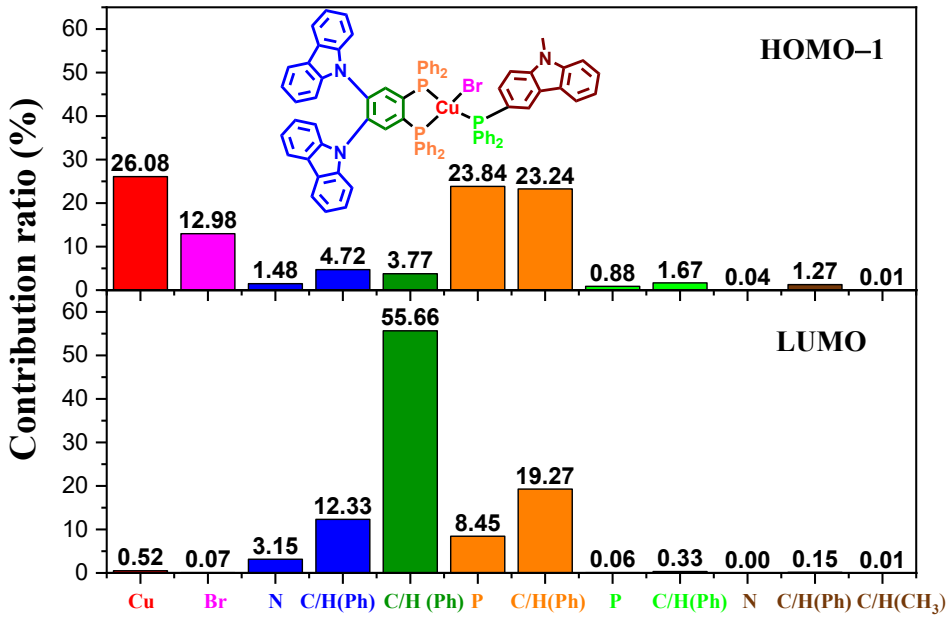

Figure S50. Compositions of the frontier molecular orbitals at optimized S_0 geometry of complex **4**.

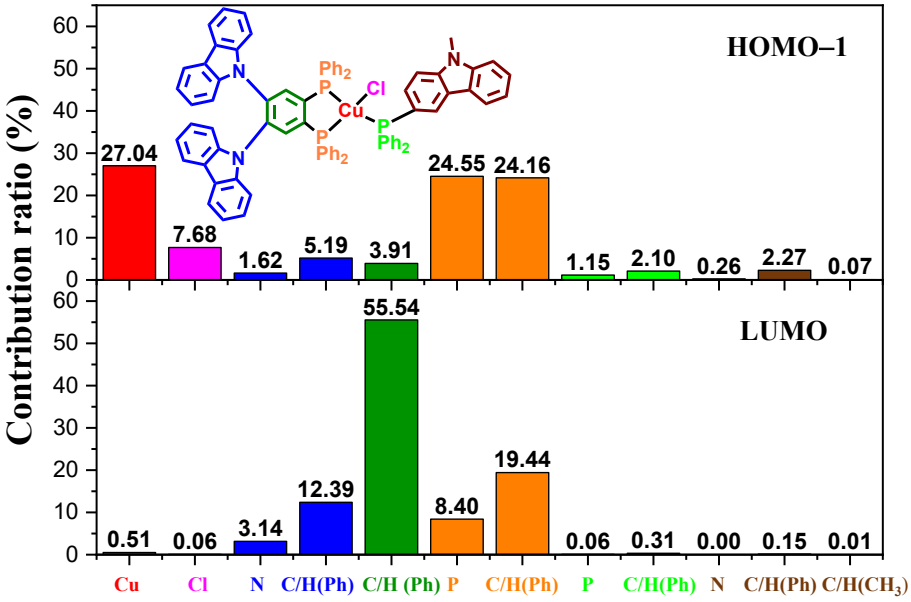

Figure S51. Compositions of the frontier molecular orbitals at optimized S_0 geometry of complex **5**.

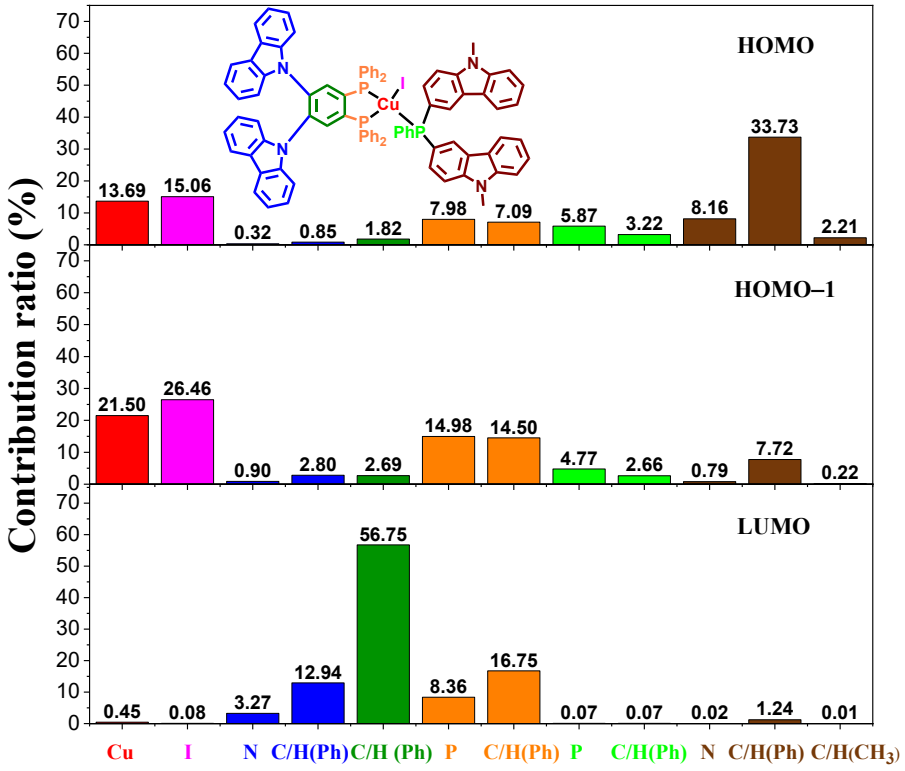

Figure S52. Compositions of the frontier molecular orbitals at optimized S_0 geometry of complex **6**.

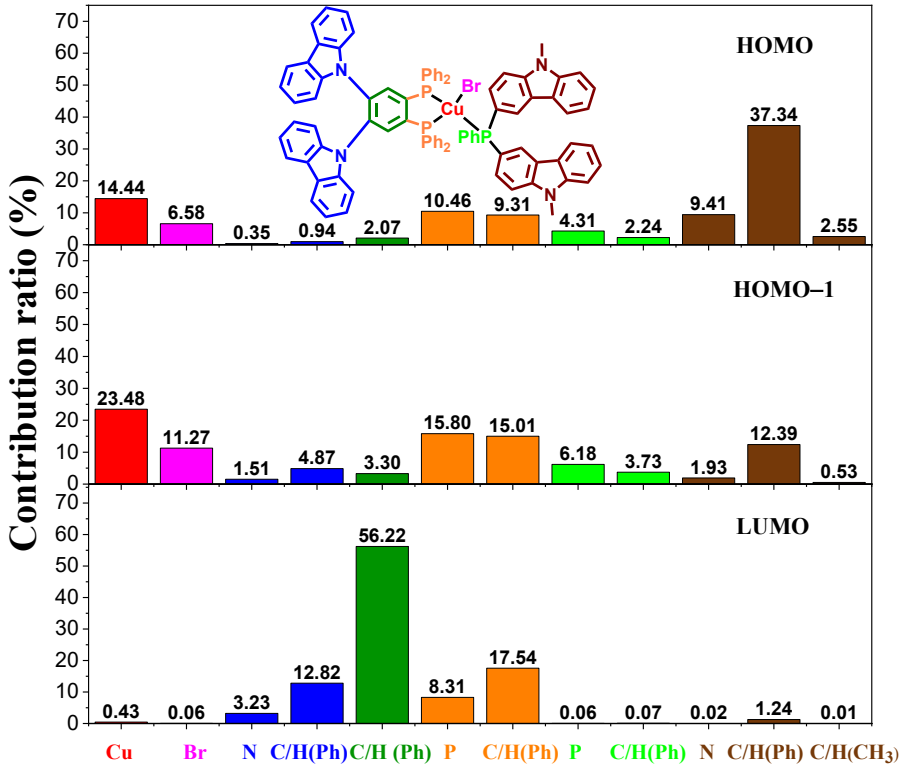

Figure S53. Compositions of the frontier molecular orbitals at optimized S_0 geometry of complex **7**.

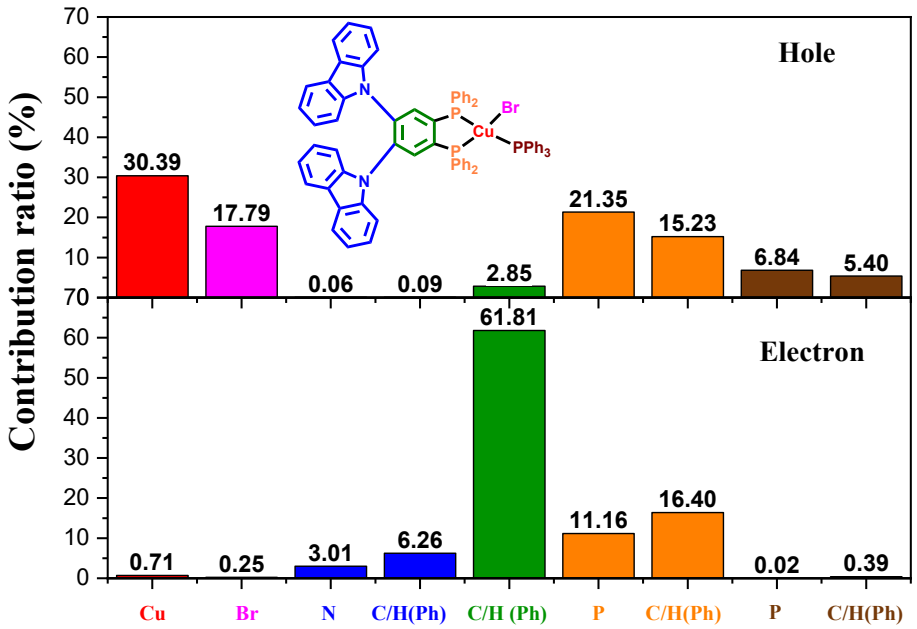

Figure S54. Compositions of the frontier natural transition orbitals at optimized S_1 geometry of complex **1**.

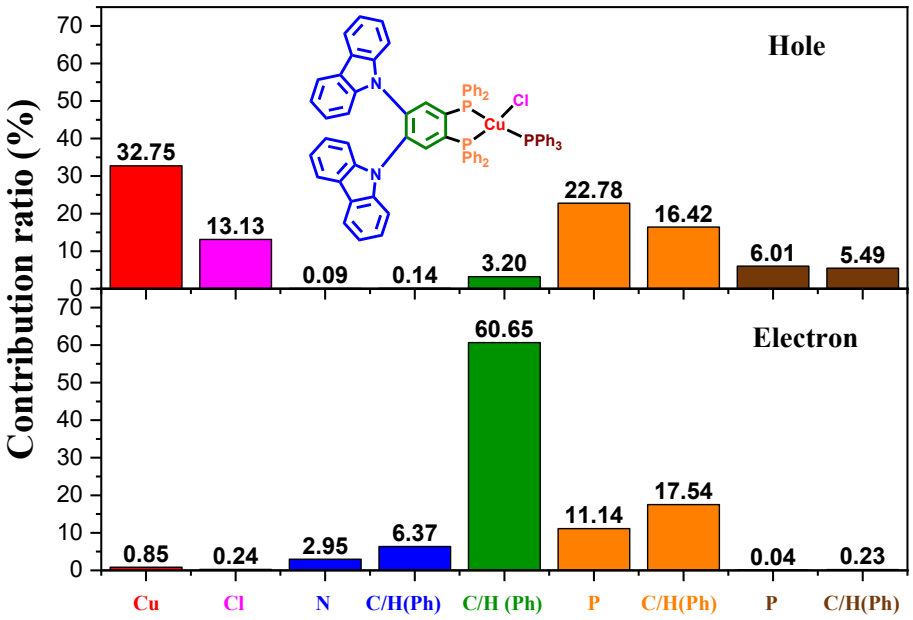

Figure S55. Compositions of the frontier natural transition orbitals at optimized S_1 geometry of complex **2**.

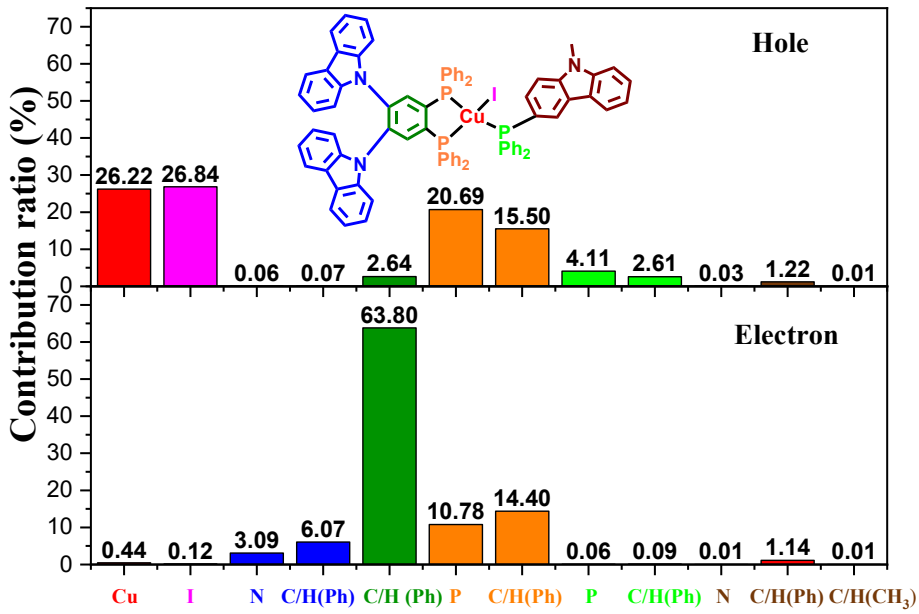

Figure S56. Compositions of the frontier natural transition orbitals at optimized S_1 geometry of complex **3**.

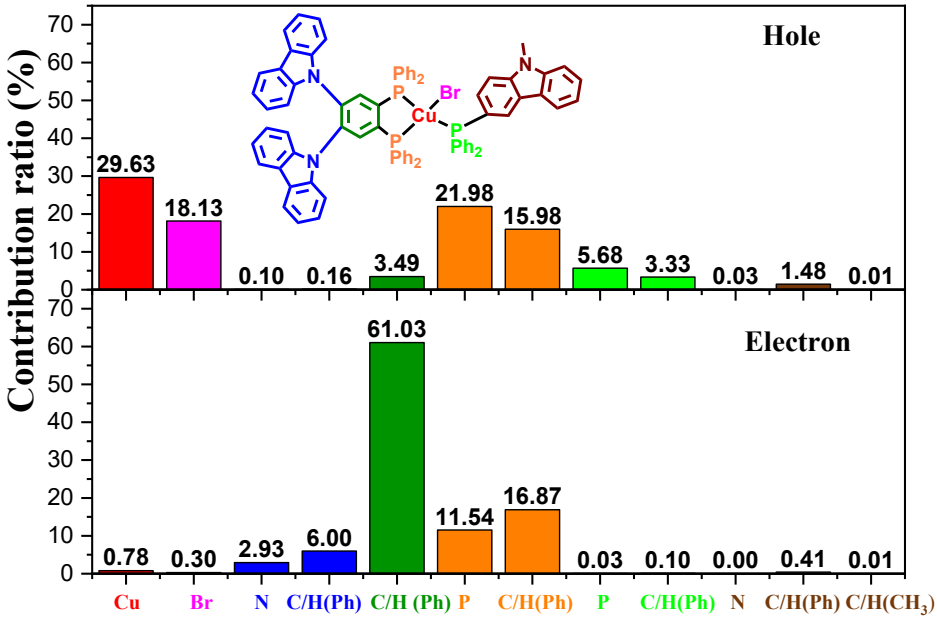

Figure S57. Compositions of the frontier natural transition orbitals at optimized S_1 geometry of complex **4**.

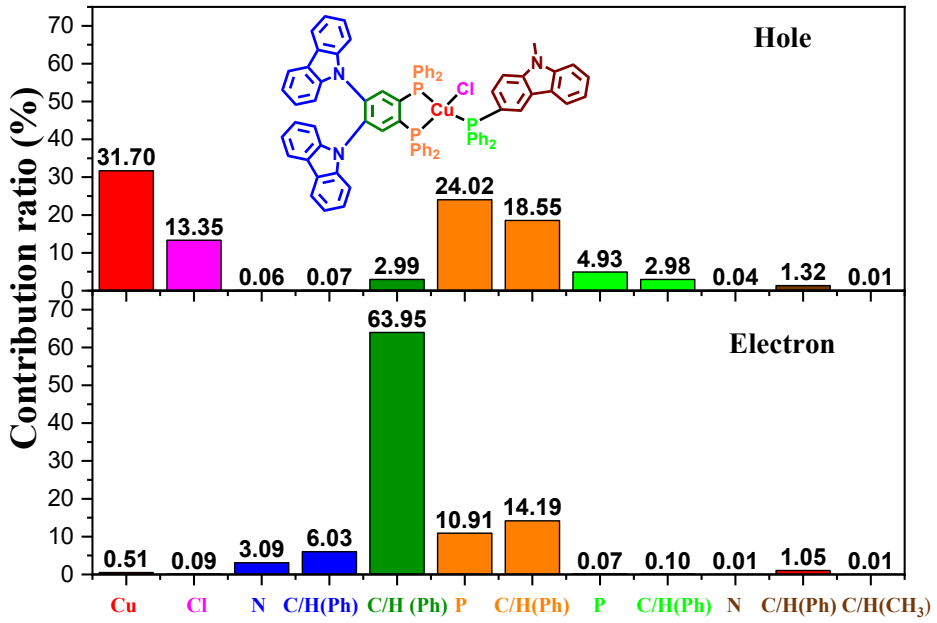

Figure S58. Compositions of the frontier natural transition orbitals at optimized S_1 geometry of complex **5**.

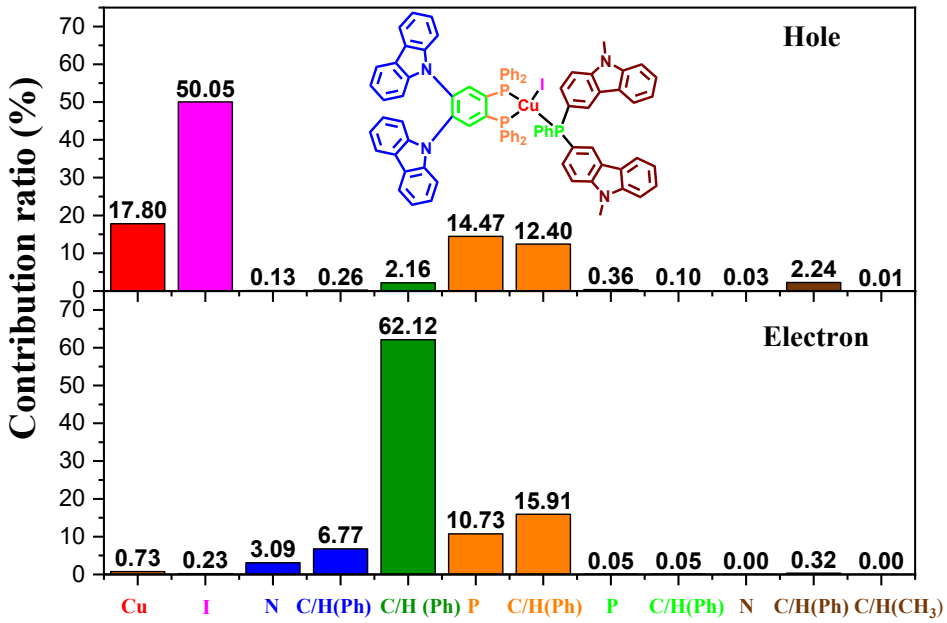

Figure S59. Compositions of the frontier natural transition orbitals at optimized S_1 geometry of complex **6**.

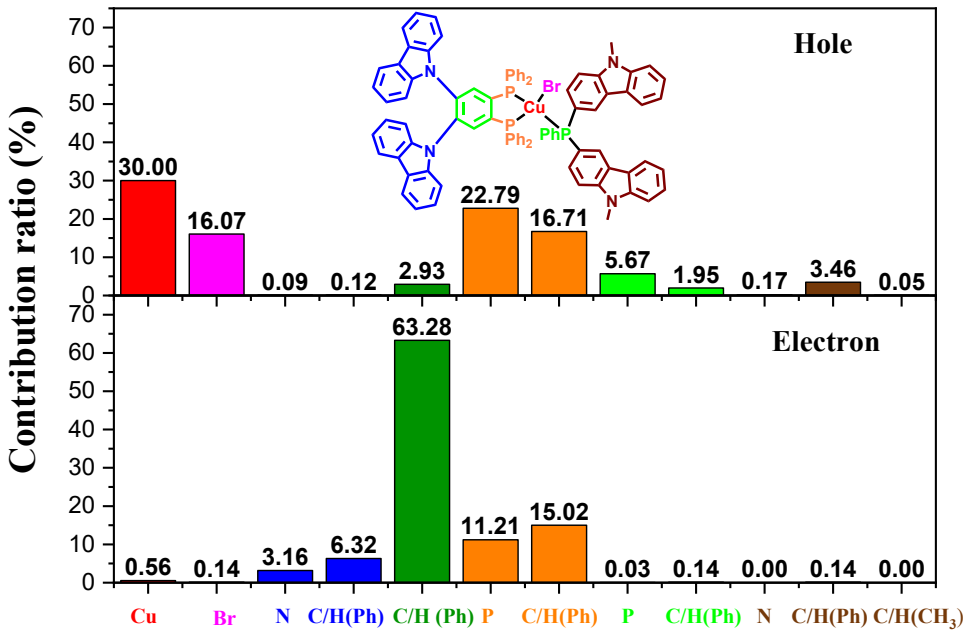

Figure S60. Compositions of the frontier natural transition orbitals at optimized S_1 geometry of complex **7**.

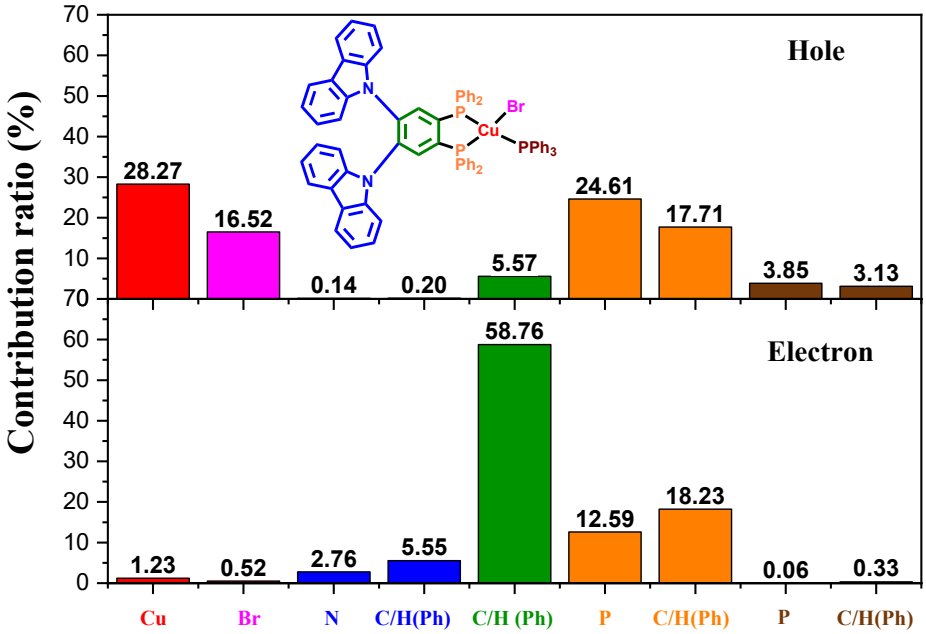

Figure S61. Compositions of the frontier natural transition orbitals at optimized T_1 geometry of complex **1**.

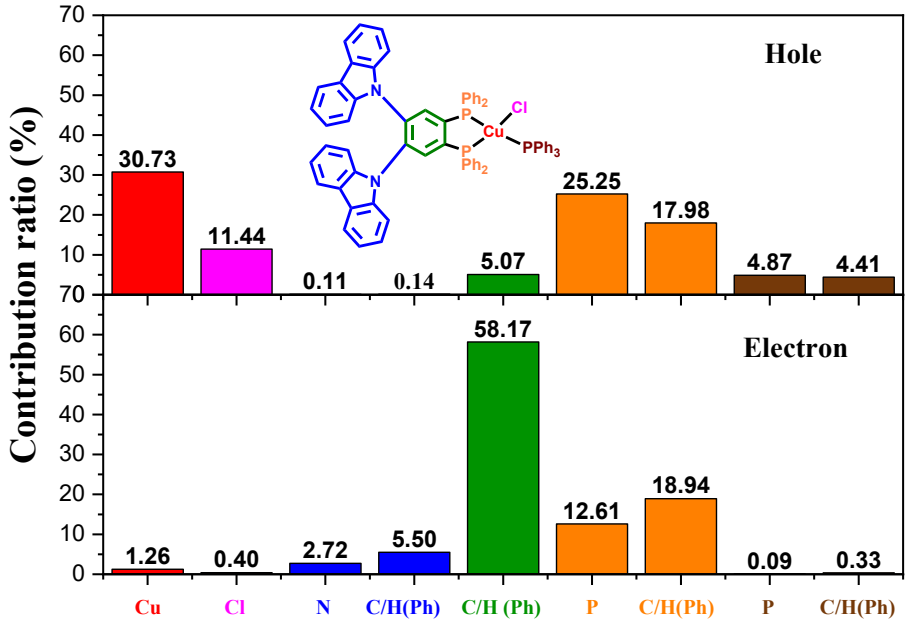

Figure S62. Compositions of the frontier natural transition orbitals at optimized T_1 geometry of complex **2**.

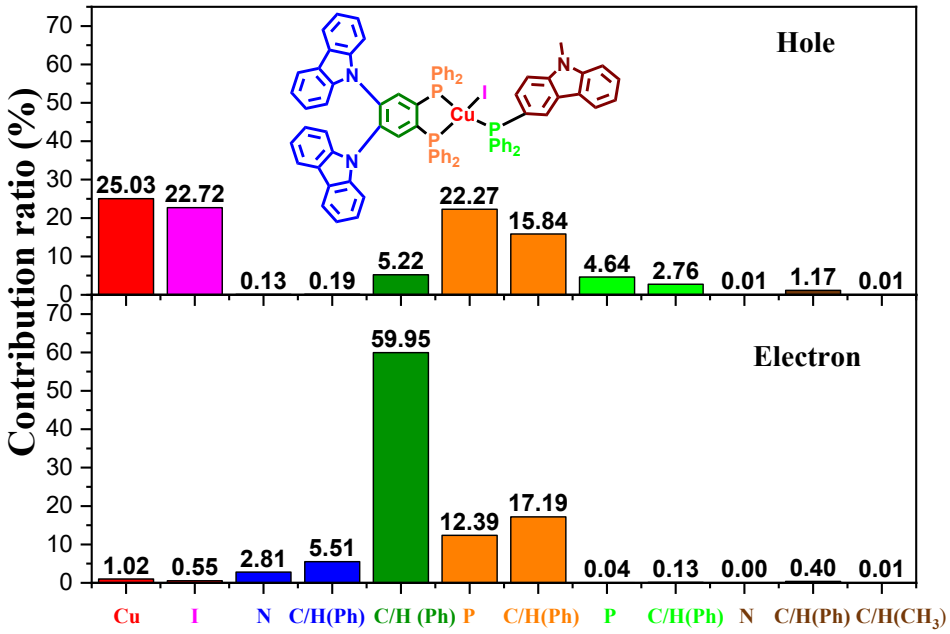

Figure S63. Compositions of the frontier natural transition orbitals at optimized T_1 geometry of complex **3**.

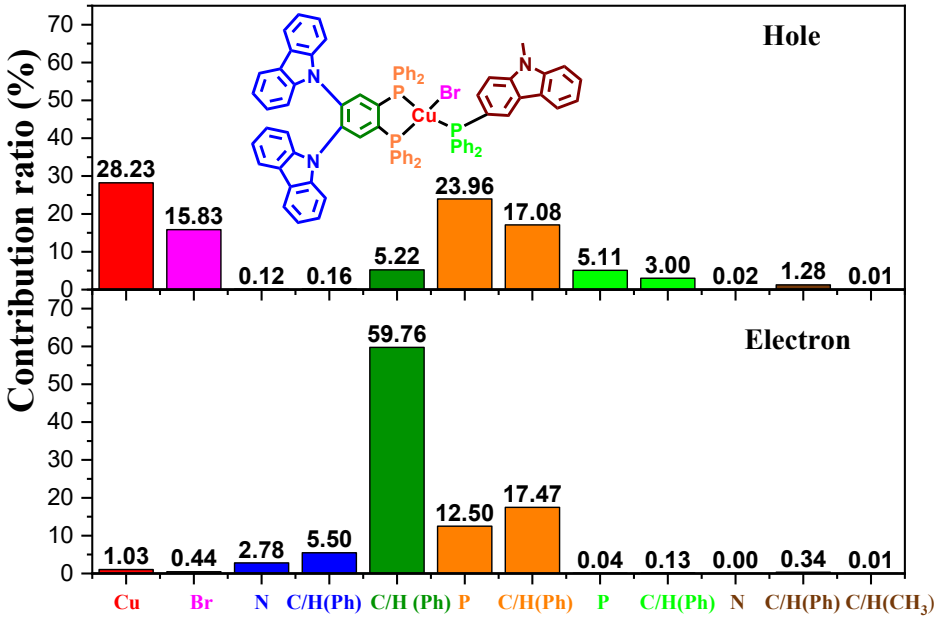

Figure S64. Compositions of the frontier natural transition orbitals at optimized T_1 geometry of complex **4**.

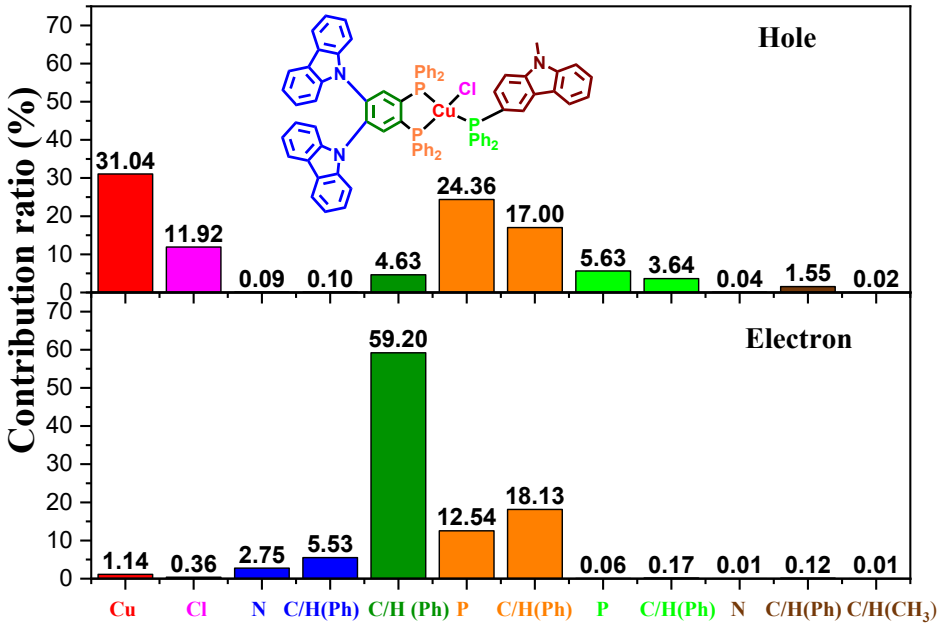

Figure S65. Compositions of the frontier natural transition orbitals at optimized T_1 geometry of complex **5**.

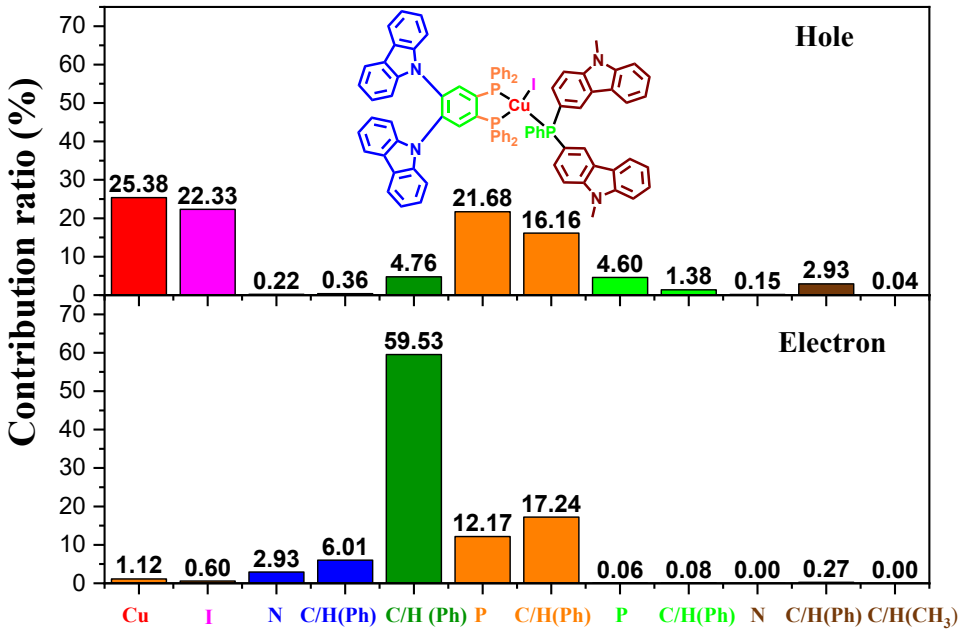

Figure S66. Compositions of the frontier natural transition orbitals at optimized T_1 geometry of complex **6**.

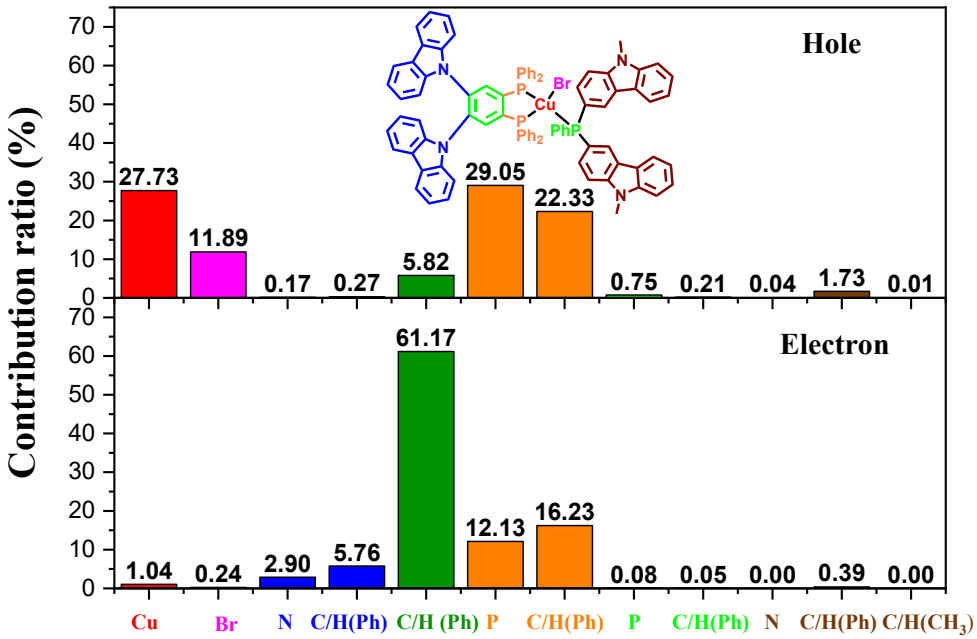

Figure S67. Compositions of the frontier natural transition orbitals at optimized T_1 geometry of complex **7**.

Complex	Geometry		
	S_0	S_1	T_1
1	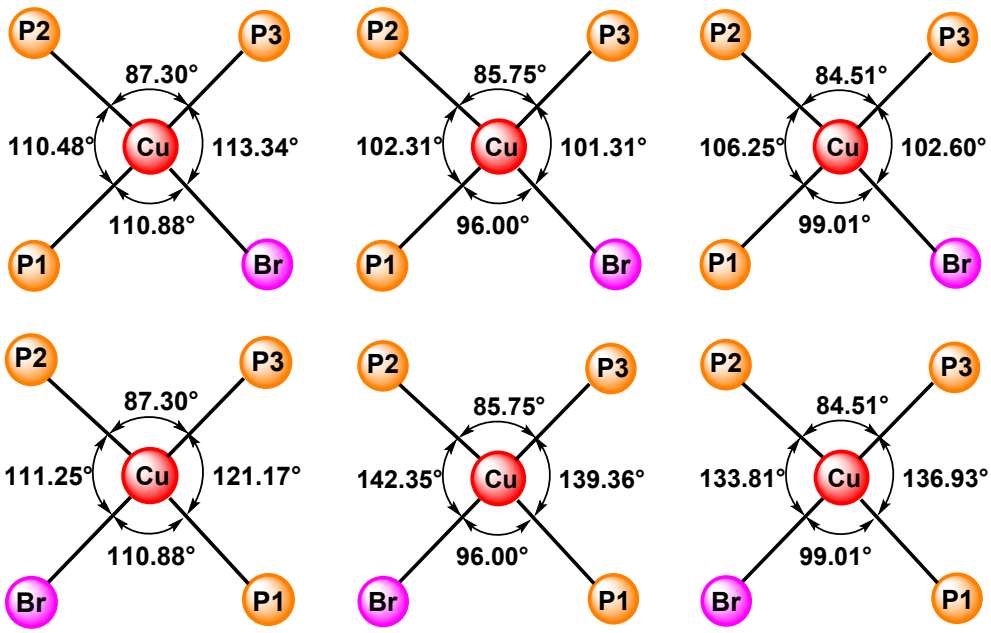		

2

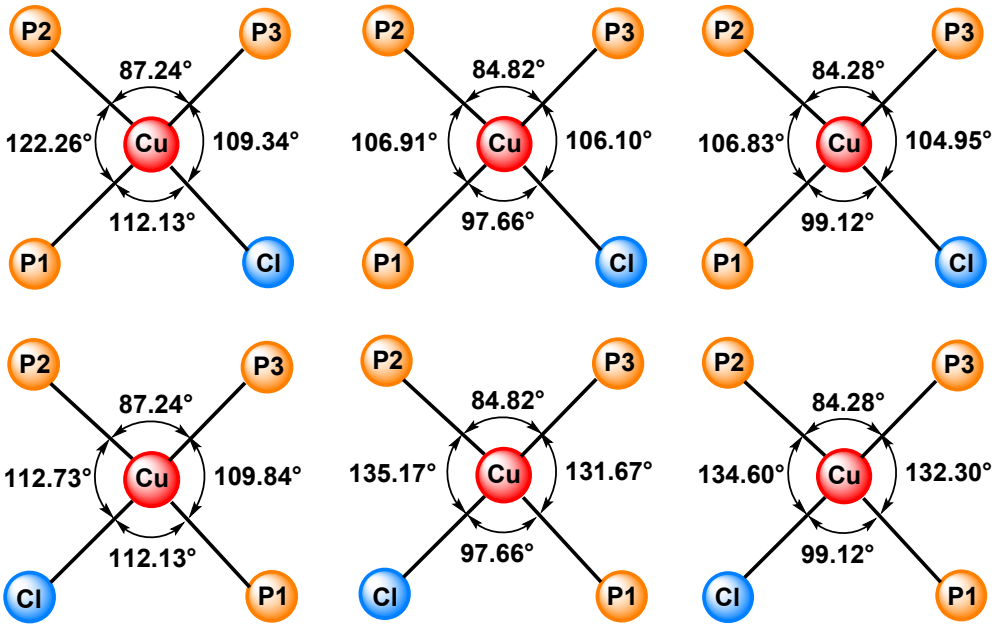
P2 P3 87.24° 122.26° Cu 109.34° 112.13° P1 Cl
P2 P3 84.82° 106.91° Cu 106.10° 97.66° P1 Cl
P2 P3 84.28° 106.83° Cu 104.95° 99.12° P1 Cl
P2 P3 87.24° 112.73° Cu 109.84° 112.13° Cl P1
P2 P3 84.82° 135.17° Cu 131.67° 97.66° Cl P1
P2 P3 84.28° 134.60° Cu 132.30° 99.12° Cl P1

3

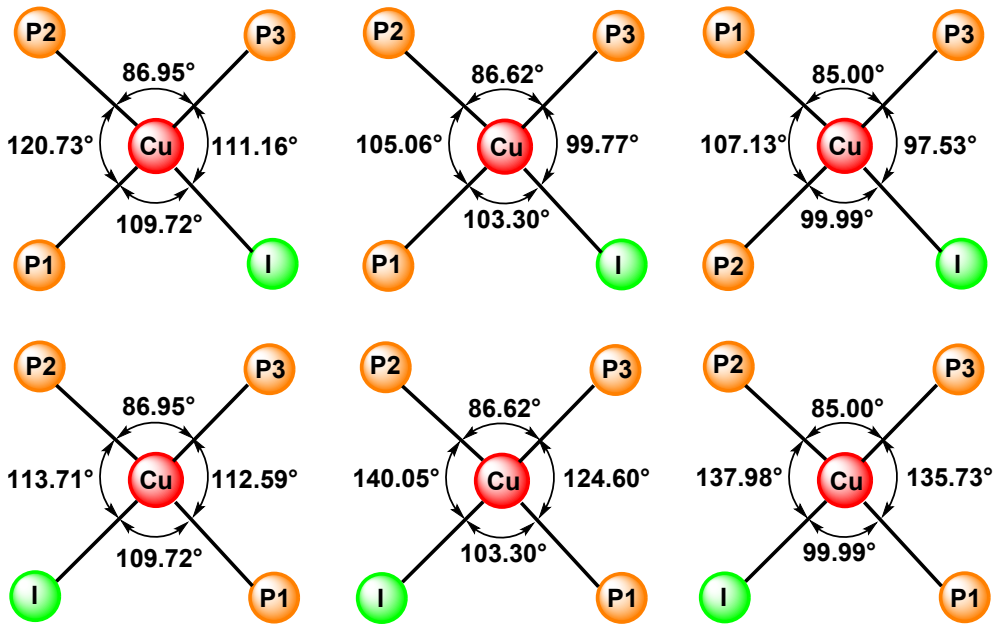
P2 P3 86.95° 120.73° Cu 111.16° 109.72° P1 I
P2 P3 86.62° 105.06° Cu 99.77° 103.30° P1 I
P1 P3 85.00° 107.13° Cu 97.53° 99.99° P2 I
P2 P3 86.95° 113.71° Cu 112.59° 109.72° I P1
P2 P3 86.62° 140.05° Cu 124.60° 103.30° I P1
P2 P3 85.00° 137.98° Cu 135.73° 99.99° I P1

4

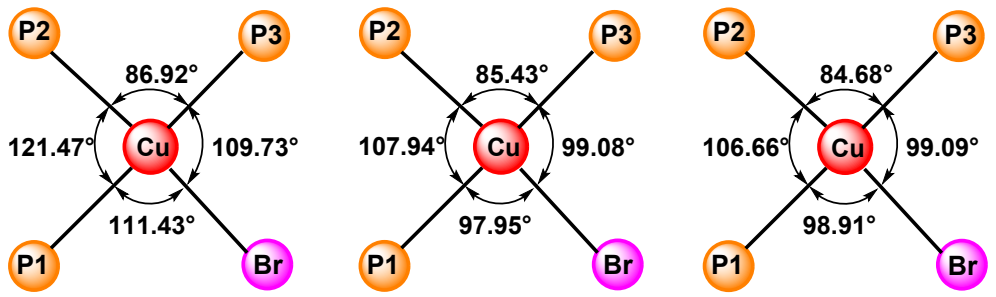
P2 P3 86.92° 121.47° Cu 109.73° 111.43° P1 Br
P2 P3 85.43° 107.94° Cu 99.08° 97.95° P1 Br
P2 P3 84.68° 106.66° Cu 99.09° 98.91° P1 Br

5

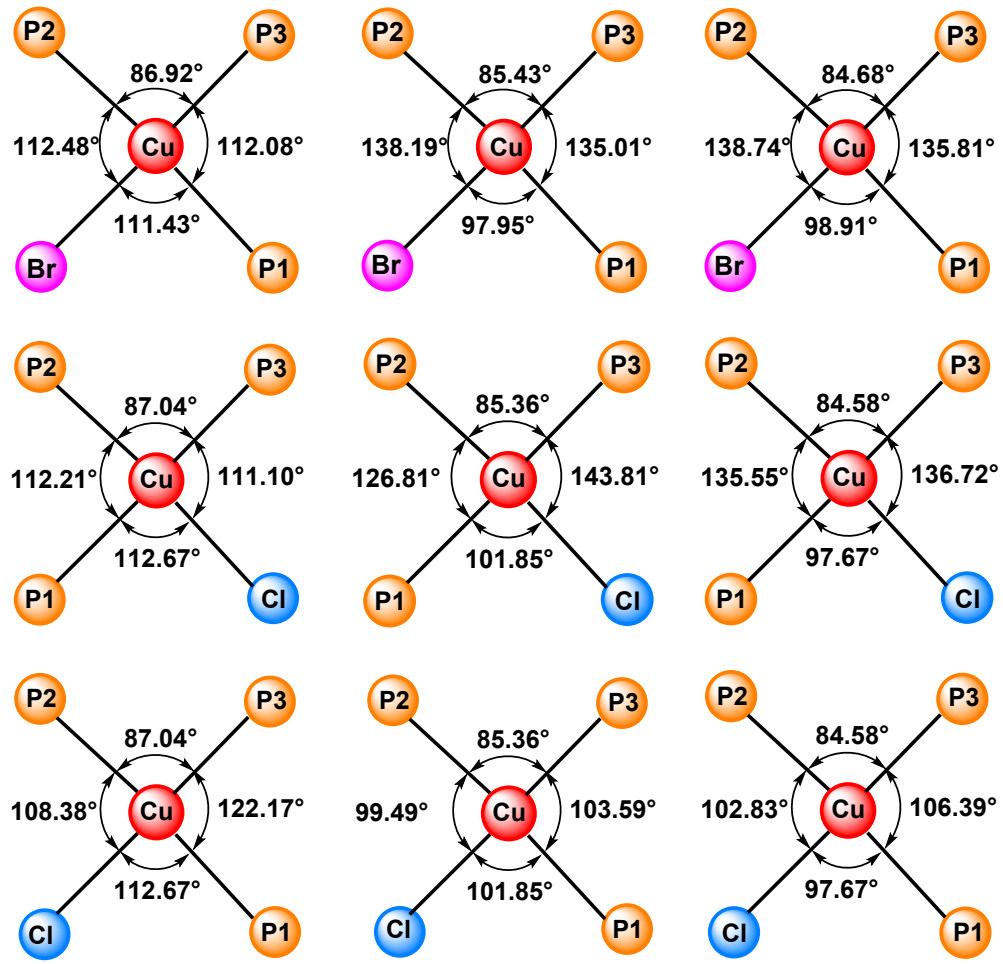
P2 P3 86.92° 112.48° Cu 112.08° 111.43° Br P1
P2 P3 85.43° 138.19° Cu 135.01° 97.95° Br P1
P2 P3 84.68° 138.74° Cu 135.81° 98.91° Br P1
P2 P3 87.04° 112.21° Cu 111.10° 112.67° P1 Cl
P2 P3 85.36° 126.81° Cu 143.81° 101.85° P1 Cl
P2 P3 84.58° 135.55° Cu 136.72° 97.67° P1 Cl
P2 P3 87.04° 108.38° Cu 122.17° 112.67° Cl P1
P2 P3 85.36° 99.49° Cu 103.59° 101.85° Cl P1
P2 P3 84.58° 102.83° Cu 106.39° 97.67° Cl P1

6

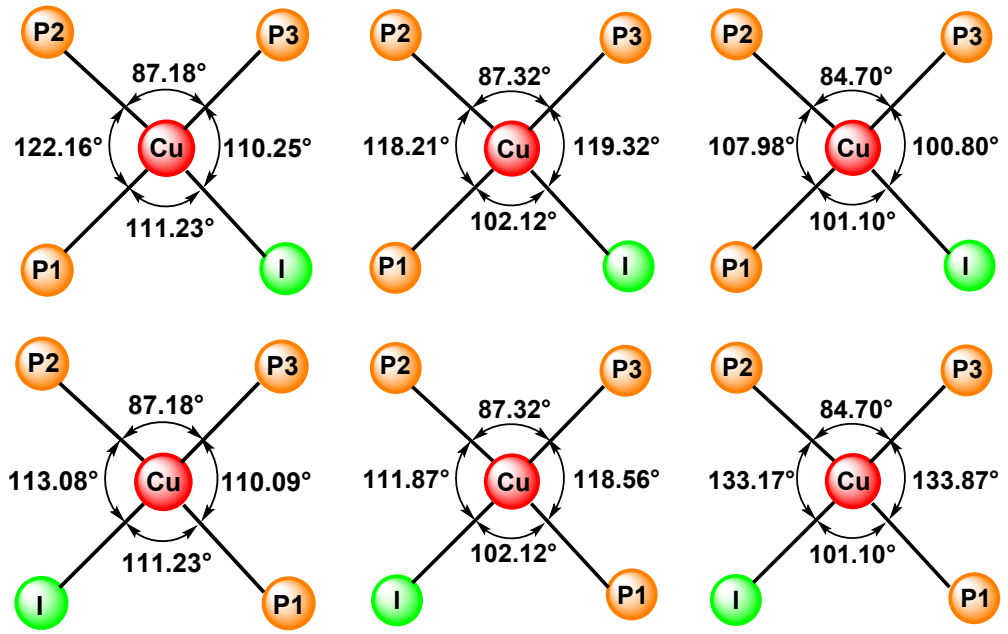
P2 P3 87.18° 122.16° Cu 110.25° 111.23° P1 I
P2 P3 87.32° 118.21° Cu 119.32° 102.12° P1 I
P2 P3 84.70° 107.98° Cu 100.80° 101.10° P1 I
P2 P3 87.18° 113.08° Cu 110.09° 111.23° I P1
P2 P3 87.32° 111.87° Cu 118.56° 102.12° I P1
P2 P3 84.70° 133.17° Cu 133.87° 101.10° I P1

7

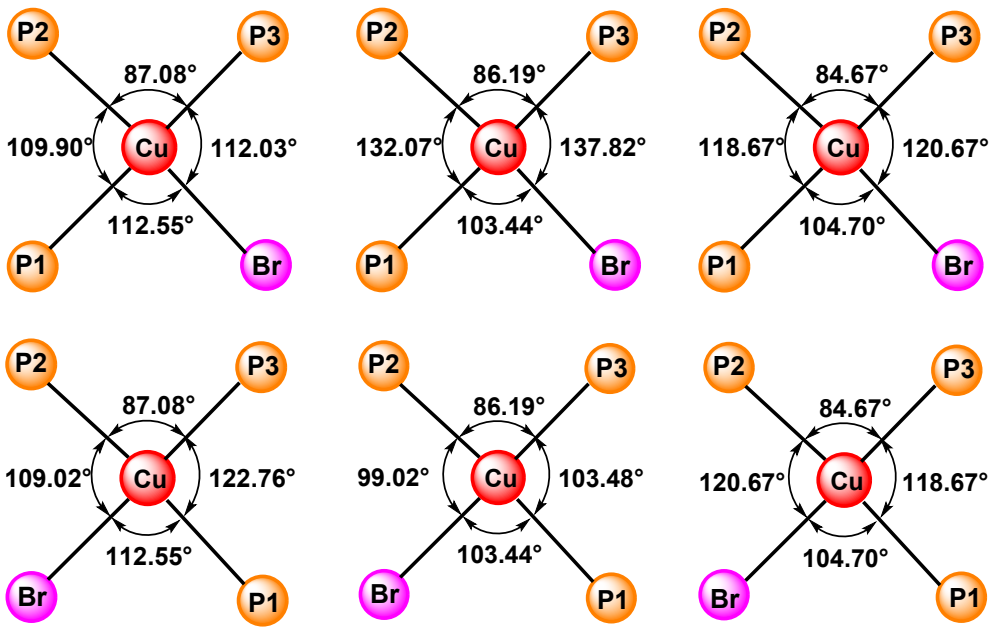

Figure S68. The core structures in the optimized S_0, S_1, and T_1 geometries for complexes **1–7**.

Table S1. Crystallographic data and details for complexes **1–7**.

	1 • CH_2Cl_2	**2** • $3(CH_2Cl_2)$
Empirical formula	$C_{72}H_{53}CuBrN_2P_3$ • CH_2Cl_2	$C_{72}H_{53}CuClN_2P_3$ • $3(CH_2Cl_2)$
Formula weight	1267.45	1392.84
Temperature (K)	100.00(10)	199.99(10)
Wavelength (Å)	1.54184	1.54184
Crystal system	Monoclinic	Triclinic
Space group	$P2_1/c$	P–1
a (Å)	10.31050(10)	10.05020(10)
b (Å)	16.27350(10)	14.4627(2)
c (Å)	37.9409(2)	24.4386(3)
α (°)	90	106.0020(10)
β (°)	94.0320(10)	95.2810(10)
γ (°)	90	97.9430(10)
V (Å^3)	6350.27(8)	3350.08(7)
Z	4	2
ρ (g cm^{-3})	1.326	1.381
μ (mm^{-1})	3.045	4.055
F (0 0 0)	2600	1432
θ range for data collection (°)	2.956 to 76.704	3.226 to 76.603
Index ranges	$-12 \leq h \leq 13$ $-18 \leq k \leq 20$ $-47 \leq l \leq 47$	$-12 \leq h \leq 12$ $-18 \leq k \leq 16$ $-30 \leq l \leq 30$
Independent reflections	12814 [R(int) = 0.0434]	13539 [R(int) = 0.1070]
Completeness to θ = 67.684°	99.5%	99.8%
Max. and min. transmission	1.00000 and 0.48555	1.00000 and 0.56699
Gof	1.046	1.101
Final R indices [I > $2\sigma(I)$]	R_1 = 0.0359 wR_2 = 0.0922	R_1 = 0.0818 wR_2 = 0.2272
R (all data)	R_1 = 0.0387 wR_2 = 0.0941	R_1 = 0.0880 wR_2 = 0.2362
Max/min (e Å^3)	0.653 and –1.072	1.338 and –1.301

	3	**4**	**5**
Empirical formula	$C_{79}H_{58}CuIN_3P_3$	$C_{79}H_{58}CuBrN_3P_3$	$C_{79}H_{58}CuClN_3P_3$
Formula weight	1332.63	1285.64	1241.18
Temperature (K)	100.00(10)	100.00(10)	100.00(10)
Wavelength (Å)	1.54184	1.54184	1.54184
Crystal system	Monoclinic	Monoclinic	Monoclinic
Space group	$P2_1/n$	$P2_1/n$	$P2_1/n$
a (Å)	13.79570(10)	13.7946(2)	13.87700(10)
b (Å)	13.57050(10)	13.5185(2)	13.53800(10)
c (Å)	38.2006(4)	37.9095(6)	37.2607(3)
α (°)	90	90	90
β (°)	96.3610(10)	96.7570(10)	97.2860(10)
γ (°)	90	90	90
V (Å^3)	7107.68(11)	7020.35(18)	6943.53(9)
Z	4	4	4
ρ (g cm^{-3})	1.245	1.216	1.187
μ (mm^{-1})	4.810	2.084	1.786
F (0 0 0)	2720	2648	2576
θ range for data collection (°)	2.328 to 76.826	3.301 to 76.830	2.391 to 76.791
Index ranges	$-15 \leq h \leq 17$ $-15 \leq k \leq 17$ $-43 \leq l \leq 48$	$-17 \leq h \leq 17$ $-17 \leq k \leq 15$ $-47 \leq l \leq 43$	$-17 \leq h \leq 17$ $-14 \leq k \leq 17$ $-44 \leq l \leq 46$
Independent reflections	14432 [R(int) = 0.0470]	14089 [R(int) = 0.0671]	14156 [R(int) = 0.0403]
Completeness to θ = 67.684°	99.9%	99.4%	99.8%
Max. and min. transmission	1.00000 and 0.73425	1.00000 and 0.51283	1.00000 and 0.90148
Gof	1.036	1.038	1.021
Final R indices [I > 2σ(I)]	R_1 = 0.0424 wR_2 = 0.1093	R_1 = 0.1005 wR_2 = 0.2436	R_1 = 0.0388 wR_2 = 0.1033
R (all data)	R_1 = 0.0455 wR_2 = 0.1115	R_1 = 0.1095 wR_2 = 0.2484	R_1 = 0.0420 wR_2 = 0.1057
Max/min (e Å^3)	1.280 and –0.810	1.314 and –0.966	0.420 and –0.374

	6 • CH_2Cl_2	**7**
Empirical formula	$C_{86}H_{63}CuIN_4P_3$ • CH_2Cl_2	$C_{86}H_{63}CuBrN_4P_3$
Formula weight	1520.68	1388.76
Temperature (K)	100.00(10)	293
Wavelength (Å)	1.54184	1.54184
Crystal system	Triclinic	Triclinic
Space group	P−1	P−1
a (Å)	10.38730(10)	10.35530(10)
b (Å)	15.8741(2)	16.0837(3)
c (Å)	24.5313(3)	24.9522(2)
α (°)	98.9400(10)	97.8150(10)
β (°)	100.9360(10)	100.9750(10)
γ (°)	97.5010(10)	97.9910(10)
V (Å^3)	3869.47(8)	3983.40(9)
Z	2	2
ρ (g cm^{-3})	1.305	1.158
μ (mm^{-1})	5.109	1.877
F (0 0 0)	1552	1432
θ range for data collection (°)	2.857 to 76.790	2.814 to 76.681
Index ranges	$-13 \leq h \leq 13$ $-20 \leq k \leq 19$ $-30 \leq l \leq 30$	$-13 \leq h \leq 13$ $-20 \leq k \leq 19$ $-26 \leq l \leq 31$
Independent reflections	15702 [R(int) = 0.0528]	16170 [R(int) = 0.0559]
Completeness to θ = 67.684°	99.8%	99.7%
Max. and min. transmission	1.00000 and 0.49493	1.00000 and 0.25038
Gof	1.042	1.062
Final R indices	R_1 = 0.0596	R_1 = 0.0453
[I > 2σ(I)]	wR_2 = 0.1620	wR_2 = 0.1325
R (all data)	R_1 = 0.0645	R_1 = 0.0517
	wR_2 = 0.1665	wR_2 = 0.1372
Max/min (e Å^3)	1.921 and −1.586	0.370 and −0.658

Table S2. Computed excitation states for complex **1** in CH_2Cl_2.

State	λ(nm)/*E*(eV)	Configurations	*f*
1	373.9 / 3.32	H→L (98)	0.0620
5	341.0 / 3.64	H-3→L (7); H-2→L (12); H-1→L+1 (77)	0.0931
6	336.4 / 3.69	H-3→L (83); H-2→L+1 (4); H-1→L+1 (10)	0.2539
9	320.3 / 3.87	H→L+3 (36); H→L+4 (40); H→L+5 (12)	0.0634
25	296.9 / 4.18	H-3→L+6 (3); H-2→L+6 (23); H-1→L+5 (9); H-1→L+6 (33); H→L+8 (21)	0.0709
73	260.6 / 4.76	H-5→L+7 (2); H-3→L+16 (3); H-2→L+11 (3); H-2→L+12 (3); H-2→L+13 (4); H-2→L+16 (19); H-2→L+17 (3); H-1→L+13 (8); H-1→L+15 (7); H-1→L+16 (23); H-1→L+17 (4)	0.0690
75	259.5 / 4.78	H-6→L+2 (3); H-6→L+3 (3); H-6→L+4 (3); H-6→L+5 (3); H-5→L+7 (12); H-4→L+4 (3); H-4→L+6 (8); H-4→L+8 (16); H-2→L+13 (5); H-2→L+15 (2); H-1→L+15 (13); H-1→L+16 (4); H→L+15 (5)	0.1330
78	258.3 / 4.80	H-6→L+7 (4); H-5→L+7 (21); H-4→L+6 (7); H-4→L+7 (3); H-4→L+8 (4); H-2→L+14 (5); H-1→L+14 (5); H-1→L+15 (13); H-1→L+16 (4); H→L+15 (9)	0.1855

Table S3. Computed excitation states for complex **2** in CH_2Cl_2.

State	λ(nm)/*E*(eV)	Configurations	*f*
1	376.7 / 3.29	H→L (98)	0.0639
3	354.7 / 3.50	H-1→L (85); H→L+1 (11)	0.0693
5	339.6 / 3.65	H-3→L (8); H-2→L (30); H-1→L+1 (58)	0.0664
6	335.8 / 3.69	H-3→L (82); H-1→L+1 (13)	0.3044
8	323.4 / 3.83	H→L+3 (61); H→L+4 (14); H→L+5 (16)	0.0742
25	295.7 / 4.19	H-3→L+6 (4); H-2→L+6 (36); H-1→L+3 (2); H-1→L+5 (6); H-1→L+6 (40); H→L+8 (3); H→L+9 (2)	0.0617
38	282.5 / 4.39	H-4→L+3 (22); H-4→L+4 (51); H-2→L+3 (3); H-2→L+4 (2); H-1→L+14 (3)	0.1021
72	259.2 / 4.78	H-5→L+2 (2); H-5→L+3 (4); H-5→L+4 (3); H-5→L+5 (4); H-4→L+5 (3); H-4→L+6 (6); H-4→L+8 (6); H-2→L+11 (2); H-2→L+13 (2); H-2→L+14 (3); H-2→L+16 (6); H-1→L+14 (6); H-1→L+15 (11); H→L+14 (11); H→L+15 (5)	0.1844
73	258.9 / 4.79	H-5→L+3 (12); H-5→L+5 (7); H-4→L+4 (2); H-4→L+5 (4); H-4→L+6 (13); H-4→L+7 (3); H-4→L+8 (12); H-1→L+14 (3); H→L+14 (18); H→L+15 (7)	0.0881
77	257.4 / 4.82	H-7→L+1 (3); H-5→L+4 (3); H-4→L+6 (2); H-3→L+14 (6); H-1→L+14 (32); H-1→L+15 (3); H→L+14 (16); H→L+15 (6); H→L+17 (2); H→L+18 (2)	0.1446

Table S4. Computed excitation states for complex **3** in CH_2Cl_2.

State	λ(nm)/*E*(eV)	Configurations	*f*
1	377.6 / 3.28	H-1→L (97)	0.0512
5	352.5 / 3.52	H-3→L (5); H-2→L (89)	0.0680
8	336.0 / 3.69	H-4→L (20); H-3→L (6); H-3→L+1 (2); H-2→L+1 (58); H→L+4 (8)	0.2306
21	313.3 / 3.96	H-2→L+3 (2); H-1→L+3 (3); H-1→L+6 (74); H-1→L+7 (8); H→L+7 (3)	0.0610
26	307.4 / 4.03	H-7→L+1 (6); H-5→L+1 (23); H-1→L+6 (4); H-1→L+7 (49); H→L+9 (4)	0.0659
50	291.1 / 4.26	H-8→L+1 (19); H-7→L+1 (5); H-5→L+2 (25); H-5→L+3 (4); H-5→L+4 (3); H-3→L+2 (7); H-1→L+11 (9); H→L+11 (4); H→L+12 (14)	0.0686
57	285.2 / 4.35	H-9→L+1 (2); H-6→L+4 (4); H-6→L+5 (72); H-4→L+4 (6); H-2→L+14 (4)	0.0897
82	272.6 / 4.55	H-9→L+5 (4); H-8→L+2 (4); H-8→L+4 (2); H-7→L+2 (4); H-5→L+7 (3); H-3→L+11 (4); H-1→L+13 (9); H-1→L+15 (7); H-1→L+16 (5); H→L+17 (30); H→L+18 (3)	0.1468

Table S5. Computed excitation states for complex **4** in CH_2Cl_2.

State	λ(nm)/*E*(eV)	Configurations	*f*
1	376.4 / 3.29	H-1→L (94); H→L (4)	0.0527
8	335.0 / 3.70	H-4→L (2); H-3→L (27); H-2→L+1 (61); H→L+4 (3)	0.2378
49	287.1 / 4.32	H-7→L+1 (2); H-6→L+2 (39); H-6→L+3 (2); H-3→L+2 (21); H→L+12 (18)	0.1419
80	270.6 / 4.58	H-4→L+8 (18); H-4→L+9 (8); H-4→L+11 (2); H-3→L+6 (3); H-3→L+8 (6); H-3→L+9 (2); H-2→L+8 (5); H-2→L+10 (6); H-1→L+16 (2); H→L+13 (3); H→L+17 (17); H→L+18 (5)	0.1184
81	270.1 / 4.59	H-6→L+6 (11); H-4→L+8 (9); H-4→L+9 (2); H-3→L+6 (3); H-2→L+8 (4); H-2→L+9 (7); H-2→L+11 (10); H-1→L+13 (3); H→L+17 (31)	0.1380
98	262.8 / 4.72	H-8→L+4 (2); H-5→L+5 (2); H-5→L+6 (9); H-5→L+7 (11); H-2→L+14 (8); H→L+13 (2); H→L+14 (41); H→L+16 (5)	0.1174

Table S6. Computed excitation states for complex **5** in CH_2Cl_2.

State	λ(nm)/*E*(eV)	Configurations	*f*
1	377.5 / 3.28	H-1→L (85); H→L (13)	0.0489
8	334.5 / 3.71	H-3→L (27); H-2→L+1 (63); H→L+4 (3)	0.2320
49	286.3 / 4.33	H-8→L+1 (7); H-6→L+2 (25); H-3→L+2 (34); H-1→L+12 (3); H→L+11 (2); H→L+12 (15)	0.1206
50	285.3 / 4.35	H-7→L+1 (4); H-5→L+4 (17); H-5→L+5 (56); H-3→L+4 (3); H-2→L+15 (2)	0.1010
77	269.7 / 4.60	H-8→L+2 (2); H-8→L+4 (3); H-6→L+6 (7); H-4→L+8 (5); H-3→L+6 (12); H-3→L+7 (4); H-3→L+8 (3); H-2→L+10 (15); H-2→L+11 (3); H→L+17 (7); H→L+18 (11)	0.1112
78	269.1 / 4.61	H-8→L+2 (2); H-6→L+6 (4); H-4→L+9 (4); H-2→L+9 (4); H-2→L+10 (4); H-2→L+11 (7); H-1→L+16 (5); H→L+16 (8); H→L+17 (39)	0.1957
98	260.9 / 4.75	H-7→L+3 (3); H-5→L+6 (4); H-2→L+12 (4); H-2→L+13 (5); H-2→L+14 (4); H-2→L+15 (5); H-1→L+13 (3); H-1→L+14 (21); H-1→L+15 (23); H-1→L+16 (4)	0.3006

Table S7. Computed excitation states for complex **6** in CH_2Cl_2.

State	λ(nm)/*E*(eV)	Configurations	*f*
1	379.8 / 3.26	H-1→L (51); H→L (44)	0.0603
5	350.3 / 3.54	H-4→L (7); H-3→L (85)	0.0693
8	335.3 / 3.70	H-5→L (18); H-4→L (11); H-4→L+1 (3); H-3→L+1 (44); H-2→L (6); H→L+2 (3); H→L+4 (3)	0.2150
11	330.3 / 3.75	H-1→L+2 (15); H-1→L+3 (12); H-1→L+4 (42); H-1→L+6 (4); H→L+2 (5); H→L+3 (3); H→L+4 (7); H→L+6 (4)	0.0781
15	323.1 / 3.84	H-5→L+1 (8); H-4→L+2 (3); H-2→L+2 (9); H-2→L+3 (4); H-2→L+4 (24); H-1→L+4 (10); H→L+6 (29)	0.0736
35	302.9 / 4.09	H-10→L (3); H-4→L+4 (4); H-1→L+5 (2); H-1→L+8 (50); H→L+9 (21)	0.0864
41	299.1 / 4.15	H-10→L (9); H-9→L (11); H-4→L+4 (5); H-1→L+8 (2); H→L+9 (24); H→L+10 (24); H→L+11 (4)	0.0637
68	285.4 / 4.34	H-11→L+1 (3); H-7→L+5 (66); H-5→L+6 (3);H-3→L+4 (2); H-3→L+6 (2); H-3→L+15 (3); H-1→L+12 (3)	0.0855
75	281.4 / 4.41	H-9→L+4 (3); H-8→L+2 (3); H-6→L+6 (13); H-5→L+4 (3); H-3→L+7 (16); H-2→L+7 (4); H-1→L+13 (6); H→L+13 (29)	0.1298
91	274.6 / 4.51	H-9→L+4 (3); H-6→L+7 (17); H-5→L+7 (6); H-4→L+9 (8); H-4→L+11 (3); H-2→L+9 (10); H-2→L+10 (11); H-2→L+11 (5); H-1→L+14 (8); H→L+14 (3); H→L+16 (2)	0.1600
92	274.3 / 4.52	H-9→L+4 (4); H-6→L+7 (9); H-5→L+6 (2); H-5→L+7 (7); H-4→L+8 (15); H-4→L+9 (2); H-4→L+10 (5); H-3→L+9 (2); H-2→L+7 (2); H-2→L+8 (2); H-2→L+10 (16); H-2→L+11 (3); H-2→L+12 (2); H-1→L+14 (3)	0.0743

Table S8. Computed excitation states for complex **7** in CH_2Cl_2.

State	λ(nm)/*E*(eV)	Configurations	*f*
1	379.3 / 3.27	H-1→L (45); H→L (51)	0.0621
4	350.2 / 3.54	H-4→L+1 (4); H-3→L (8); H-2→L (6); H-2→L+1 (8); H-1→L+1 (43); H→L+1 (27)	0.0753
7	337.9 / 3.67	H-5→L (25); H-4→L (11); H-3→L+1 (10); H-2→L+1 (7); H→L+3 (36)	0.0767
8	334.1 / 3.71	H-5→L (11); H-4→L (16); H-4→L+1 (3); H-3→L+1 (33); H-2→L+1 (26); H→L+1 (2)	0.2121
10	328.3 / 3.78	H-5→L (2); H-4→L (2); H-2→L (4); H-2→L+4 (3); H-1→L+3 (39); H-1→L+4 (10); H-1→L+6 (3); H→L+4 (21); H→L+6 (5)	0.0752
23	312.2 / 3.97	H-1→L+7 (23); H→L+2 (2); H→L+7 (62)	0.0729
60	285.3 / 4.35	H-10→L+1 (4); H-6→L+5 (74)	0.0830
63	284.1 / 4.36	H-8→L+3 (6); H-7→L+3 (3); H-5→L+7 (3); H-4→L+2 (3); H-4→L+6 (3); H-4→L+7 (13); H-3→L+7 (3); H-2→L+6 (2); H-2→L+7 (39); H-2→L+8 (2); H→L+13 (4)	0.1071
70	280.4 / 4.42	H-9→L+3 (24); H-9→L+4 (13); H-8→L+4 (7); H-7→L+3 (7); H-5→L+4 (5); H-4→L+6 (15); H-3→L+6 (2); H→L+12 (5); H→L+13 (6)	0.1135
85	273.5 / 4.53	H-9→L+4 (9); H-9→L+6 (2); H-8→L+4 (7); H-8→L+6 (2); H-6→L+3 (7); H-5→L+6 (3); H-5→L+8 (3); H-4→L+7 (2); H-4→L+8 (7); H-3→L+7 (3); H-3→L+8 (11); H-3→L+9 (4); H-2→L+7 (4); H-2→L+9 (5); H-2→L+10 (8)	0.1403
87	272.9 / 4.54	H-9→L+6 (9); H-8→L+4 (3); H-8→L+6 (5); H-5→L+6 (3); H-4→L+8 (5); H-4→L+10 (3); H-3→L+7 (2); H-2→L+8 (2); H-2→L+9 (2); H-2→L+10 (6); H-2→L+11 (3); H-1→L+14 (14); H-1→L+15 (6); H→L+16 (3); H→L+17 (7)	0.1105

6. References

(1) W. Xu, B. Chen, L. Liu, X. X. Zhong, G. J. Zhou, F. B. Li, H. M. Qin. *J. Lumin.,* 2024, **266**, 120257.

(2) L. Liu, X. Chen. CN111233924A, 2020.

(3) *SAINT Reference Manual*, Siemens Energy and Automation, Madison, WI, 1994.

(4) G. M. Sheldrick, *SADABS*, *Empirical Absorption Correction Program*, University of Göttingen, Göttingen, Germany, 1997.

(5) G. M. Sheldrick, *SHELXTL Reference Manual*, *Version 5.1*, Siemens Energy and Automation, Madison, WI, 1997.

(6) M. J. Frisch, G. W. Trucks, H. B. Schlegel, G. E. Scuseria, M. A. Robb, J. R. Cheeseman, G. Scalmani, V. Barone, G. A. Petersson, H. Nakatsuji, X. Li, M. Caricato, A. V. Marenich, J. Bloino, B. G. Janesko, R. Gomperts, B. Mennucci, H. P. Hratchian, J. V. Ortiz, A. F. Izmaylov, J. L. Sonnenberg, D. Williams-Young, F. Ding, F. Lipparini, F. Egidi, J. Goings, B. Peng, A.

Petrone, T. Henderson, D. Ranasinghe, V. G. Zakrzewski, J. Gao, N. Rega, G. Zheng, W. Liang, M. Hada, M. Ehara, K. Toyota, R. Fukuda, J. Hasegawa, M. Ishida, T. Nakajima, Y. Honda, O. Kitao, H. Nakai, T. Vreven, K. Throssell, J. A. Montgomery, Jr., J. E. Peralta, F. Ogliaro, M. J. Bearpark, J. J. Heyd, E. N. Brothers, K. N. Kudin, V. N. Staroverov, T. A. Keith, R. Kobayashi, J. Normand, K. Raghavachari, A. P. Rendell, J. C. Burant, S. S. Iyengar, J. Tomasi, M. Cossi, J. M. Millam, M. Klene, C. Adamo, R. Cammi, J. W. Ochterski, R. L. Martin, K. Morokuma, O. Farkas, J. B. Foresman, and D. J. Fox, *Gaussian 16*, *Revision A.03*, Gaussian Inc., Wallingford CT, 2016.

(7) T. Lu, F. W. Chen, *Acta Chim. Sinica,* 2011, **69**(20), 2393-2406.

(8) T. Lu, F. W. Chen, *J. Comput. Chem.,* 2012, **33**(5), 580-592.